

General relativistic MHD simulations of non-thermal flaring in Sagittarius A*

K. Chatterjee¹*, S. Markoff^{1,2}, J. Neilsen³, Z. Younsi^{4,5}, G. Witzel⁶, A. Tchekhovskoy⁷, D. Yoon¹, A. Ingram⁸, M. van der Klis¹, H. Boyce⁹, T. Do¹⁰, D. Haggard⁹ & M. A. Nowak¹²

¹Anton Pannekoek Institute for Astronomy, University of Amsterdam, Science Park 904, 1098 XH Amsterdam, The Netherlands

²Gravitation Astroparticle Physics Amsterdam (GRAPPA) Institute, University of Amsterdam, Science Park 904, 1098 XH Amsterdam, The Netherlands

³Department of Physics, Villanova University, 800 Lancaster Avenue, Villanova, PA 19085, USA

⁴Mullard Space Science Laboratory, University College London, Holmbury St. Mary, Dorking, Surrey, RH5 6NT, United Kingdom

⁵Institut für Theoretische Physik, Goethe-Universität Frankfurt, Max-von-Laue-Straße 1, D-60438 Frankfurt am Main, Germany

⁶Max Planck Institute for Radio Astronomy, Auf dem Hügel 69, D-53121 Bonn (Endenich), Germany

⁷Center for Interdisciplinary Exploration & Research in Astrophysics (CIERA), Physics & Astronomy, Northwestern University, Evanston, IL 60202, USA

⁸Department of Physics, Astrophysics, University of Oxford, Denys Wilkinson Building, Keble Road, Oxford, OX1 3RH, UK

⁹McGill Space Institute and Department of Physics, McGill University, 3600 rue University, Montreal, QC H3A 2T8, Canada

¹⁰UCLA Galactic Center Group, Physics and Astronomy Department, University of California, Los Angeles, CA 90024, USA

¹¹Department of Physics, Washington University, CB 1058, One Brookings Drive, St. Louis, MO 63130-4899, USA

Accepted XXX. Received YYY; in original form ZZZ

ABSTRACT

Sgr A* exhibits regular variability in its multiwavelength emission, including daily X-ray flares and almost continuous near-infrared (NIR) flickering. The origin of this variability is still ambiguous since both inverse Compton and synchrotron emission are possible radiative mechanisms. The underlying particle distributions are also not well constrained, particularly the non-thermal contribution. In this work, we extend previous studies of flare flux distributions employing 3D general relativistic magnetohydrodynamics (GRMHD) simulations of accreting black holes using the GPU-accelerated code H-AMR to higher resolutions than previously attempted for Sgr A*. We use the general relativistic ray-tracing (GRRT) code BHOSSE to perform the radiative transfer, assuming a hybrid thermal+non-thermal electron energy distribution. We extract ~ 60 hr lightcurves in the sub-millimetre, NIR and X-ray wavebands and, for the first time, compare the power spectra and the cumulative flux distributions of the lightcurves to statistical descriptions for Sgr A* flares. Our results indicate that non-thermal populations of electrons arising from turbulence-driven reconnection in weakly magnetised accretion flows lead to moderate NIR and X-ray flares and reasonably describe the X-ray flux distribution while fulfilling multiwavelength flux constraints. These models exhibit high rms% amplitudes, $\gtrsim 150\%$ both in the NIR and the X-rays, with changes in the accretion rate driving the 230 GHz flux variability, in agreement with Sgr A* observations.

Key words: galaxies: black hole physics – accretion, accretion discs, jets – galaxies: individual (Milky Way: Sgr A*) – magnetohydrodynamics (MHD) – methods: numerical

1 INTRODUCTION

The extreme physical conditions in the vicinity of accreting black holes (BHs) present a unique opportunity to study the acceleration of particles at energies unattainable on Earth. Magnetised plasma turbulence, instabilities, and shocks occurring naturally in accretion flows and outflows all are possible processes that trigger par-

ticle acceleration. Sagittarius A* (Sgr A*), the supermassive BH (SMBH) at the centre of our galaxy, due to its proximity, presents an excellent opportunity to test current theories about particle acceleration near black holes against high-quality observational data. Rapid fluctuations in the X-rays from this object could arise from particle acceleration near the BH (e.g., [Markoff 2005](#)). Intensive monitoring of Sgr A* has led to accurate measurements of stellar orbits yielding a BH mass of $M_{\text{BH}} = 4.1 \times 10^6 M_{\odot}$ ([Ghez et al. 2005](#); [Gillessen et al. 2017](#); [Gravity Collaboration et al. 2018a](#)) at

* E-mail: k.chatterjee@uva.nl

a distance of $D_{\text{BH}} = 8.15$ kpc (e.g., [Ghez et al. 2008](#); [Boehle et al. 2016](#); [Reid et al. 2019](#)) from the Earth, and resulted in a systematic study of its emission in the radio, millimeter (mm), near-infrared (NIR) and X-ray wavebands (e.g., see [Genzel et al. 2010](#), and references therein). Sgr A* is a remarkably faint SMBH (luminosity $L_{\text{bol}} \sim 10^{-9} L_{\text{Edd}}$, where L_{Edd} is the Eddington luminosity) that accretes gas at an estimated rate of $\dot{M} \sim 10^{-9} - 10^{-7} M_{\odot} \text{ yr}^{-1}$ ([Bower et al. 2003](#); [Marrone et al. 2007](#); [Wang et al. 2013](#)). Almost 99% of the accreted gas at the Bondi scale is lost due to turbulence by the time the flow reaches the black hole ([Wang et al. 2013](#)). At such a low accretion rate the accretion flow can be expected to be radiatively inefficient (e.g., [Yuan et al. 2003](#); also see [Yuan & Narayan 2014](#) and references therein). In spite of its low luminosity, Sgr A* is one of our best opportunities to study a SMBH via its interaction with accreting material, and it plays a crucial role in our understanding of extreme gravitational environments.

Observations at multiple wavelengths over the previous two decades have constrained the quiescent spectrum of Sgr A*. In the sub-millimetre (sub-mm) band, [Bower et al. \(2019\)](#) found a spectral index of $\alpha_{\nu} \simeq -0.31$ (where the flux density is $F_{\nu} \propto \nu^{\alpha_{\nu}}$) with the peak flux lying between 1 and 2 THz. Using a thermal synchrotron emission model to account for both the sub-mm and the NIR flux, [Bower et al. \(2019\)](#) estimates an electron temperature of $T_e \simeq 10^{11}$ K along with a small magnetic field strength of $\sim 10 - 50$ G in the inner accretion flow, consistent with previous semi-analytic results (e.g., [Falcke et al. 2000](#); [Yuan et al. 2002](#)). In the quiescent state, the X-rays seem to be dominated by thermal bremsstrahlung from the Bondi-scale accretion flow (e.g., [Quataert 2002](#); [Baganoff et al. 2003](#); [Yuan et al. 2003](#); [Connors et al. 2017](#)).

Apart from its low-luminosity quiescent state, Sgr A* regularly displays fluctuations in flux across multiple frequencies, most prominently in the NIR and X-ray bands, which are often correlated with each other (e.g., [Eckart et al. 2004](#); [Dodds-Eden et al. 2009](#); [Boyce et al. 2019](#)). Ever since [Baganoff et al. \(2001\)](#) reported the first detection of an X-ray flaring event in Sgr A* with the *Chandra X-ray Observatory*, the SMBH has been the target of multiple observational campaigns (e.g., the 3 Ms 2012 *Chandra* X-ray Visionary Project¹ and the *Swift* monitoring campaign; [Degenaar et al. 2015](#)). Recently, [Do et al. \(2019\)](#) and [Haggard et al. \(2019\)](#) reported the largest flares yet detected from Sgr A* at $2.12 \mu\text{m}$ (NIR) with the Keck Telescope and in the 2-8 keV energy band (X-ray) with *Chandra*, respectively. Further, *NuSTAR* observations confirmed that Sgr A* X-ray flares have higher energy extensions (e.g., [Barrière et al. 2014](#)) with a luminosity of $L(3\text{-}79 \text{ keV}) \sim (0.7 - 4.0) \times 10^{35} \text{ erg s}^{-1}$ and photon index $\Gamma = 2.2 \pm 0.1$ ([Zhang et al. 2017](#)) similar to the 2-8 keV *Chandra* [Nowak et al. \(2012\)](#) photon index ($\Gamma \simeq 2.0$). The X-ray emission of Sgr A* is the lowest among observed low-luminosity SMBHs, allowing the detection of low-flux stochastic flaring events in the innermost regions of the accretion flow. It is still an open question of whether this is due to the absence of a pronounced jet feature that usually dominates the X-ray emission in other accreting SMBHs. The immense amount of observational data allows us to investigate these pivotal questions about the plasma conditions in Sgr A*.

Most semi-analytical studies are agnostic about the exact mechanism behind particle acceleration in Sgr A* (e.g., [Quataert & Narayan 1999](#); [Özel et al. 2000](#); [Markoff et al. 2001](#); [Yuan et al. 2003](#); [Connors et al. 2017](#)), whether it be from shocks or magnetic reconnection. Non-thermal synchrotron emission is generally more

favoured over synchrotron-self-Compton (SSC) to be the source of simultaneous NIR and X-ray flaring events, though it is difficult to statistically differentiate between the flare flux distributions from the two models ([Dibi et al. 2016](#)). Furthermore, [Dibi et al. \(2016\)](#) shows that the large difference between the slopes of NIR and X-ray cumulative distribution functions is not well described by simpler synchrotron scenarios and leaves the door open for a fuller exploration of models involving both SSC from a thermal electron population and synchrotron from a non-thermal electron population. In non-thermal flare models, cooling of synchrotron electrons plays a vital role in reproducing the steepening in the spectral slope from NIR to X-ray (e.g., [Dodds-Eden et al. 2009, 2010](#); [Dibi et al. 2014](#); [Ponti et al. 2017](#)). This idea gained even more traction with the recent [Gravity Collaboration et al. \(2018b\)](#) detection of three NIR flares consistent with a hotspot orbiting at a distance of $\sim 6 - 10$ gravitational radii ($r_g \equiv GM_{\text{BH}}/c^2$, where G and c are the gravitational constant and the speed of light respectively) from the BH with an inclination of approximately 140° degrees and an orbital period ~ 115 minutes ([Gravity Collaboration et al. 2020b](#)). This detection points towards localised mechanisms such as magnetic reconnection and electron heating behind the NIR flaring. However, for the large NIR flare reported in [Do et al. \(2019\)](#), the authors suggest that an increase in the accretion rate could explain the exceptionally high flux. This naturally raises the question if there are alternative mechanisms that can lead to such changes in the NIR emission. Indeed, recent work by [Gutiérrez et al. \(2020\)](#) demonstrates that large NIR flares could have a non-thermal origin in a magnetised blob of plasma, i.e., a plasmoid. Local particle-in-cell simulations show that plasmoids can naturally form as a result of relativistic magnetic reconnection in environments that are prevalent in accretion disks as well as the jet boundary (e.g., [Sironi et al. 2015](#); [Ball et al. 2018](#)), but whether such plasmoids grow to the sizes required to explain the enormous flux is not yet known. The computational demands of these simulation prohibits the exploration of bulk flow effects on the microscopic plasmoid behaviour, requiring alternate schemes to incorporate the global turbulence of the accretion flows.

Over the past decades, the theoretical astrophysics community has increasingly used general relativistic magnetohydrodynamic (GRMHD) simulations of accreting BHs to produce a more self-consistent description of accretion dynamics. GRMHD simulations usually employ the single fluid approximation, assuming that the ion temperature dominates the flow temperature. Therefore, we require a model that describes the electron temperature in postprocessing (e.g., [Howes 2010](#); [Rowan et al. 2017](#); [Werner et al. 2018](#)). Along with GRMHD quantities, the choice of the electron temperature model is important to generate multiwavelength spectra using general relativistic ray-tracing (GRRT) codes, and thus, enable us to compare simulated data to the observed spectrum of Sgr A* (e.g., [Dexter et al. 2009](#); [Mościbrodzka et al. 2009](#); [Dexter et al. 2010](#); [Dibi et al. 2012](#); [Shevchenko et al. 2012](#); [Drappeau et al. 2013](#); [Mościbrodzka & Falcke 2013](#); [Chan et al. 2015](#); [Davelaar et al. 2018](#); [Anantua et al. 2020](#)). An alternative approach is to evolve the electron thermodynamics along with the gas evolution self-consistently within a GRMHD simulation (e.g., [Ressler et al. 2015](#); [Ryan et al. 2017](#); [Chael et al. 2018](#); [Dexter et al. 2020b](#)).

Using the robust framework of GRMHD+GRRT methods, quite a few studies have tried to investigate the properties of the accretion flow that lead to flares. The 2D GRMHD simulations in [Drappeau et al. \(2013\)](#) consider thermal SSC origins of X-ray flaring. [Chan et al. \(2015\)](#) was the first to use 3D GRMHD simulations that invoke thermal bremsstrahlung emission to model undet-

¹ <http://www.sgra-star.com>

tected X-ray flares ($\lesssim 10\%$ of the quiescent X-ray flux; [Neilsen et al. 2013](#)), thought to come from the inner accretion flow. Further, the simulations of [Ball et al. \(2016\)](#) in 3D and [Davelaar et al. \(2018\)](#) in 2D use a hybrid thermal+non-thermal synchrotron model ([Özel et al. 2000](#)) and a κ -distribution model, respectively, to study Sgr A*'s X-ray emission. However, the 2D restriction and the low resolution of these simulations might result in spurious numerical artefacts. Indeed, very recently, [Dexter et al. \(2020a\)](#) and [Porth et al. \(2020\)](#) employed high resolution 3D GRMHD simulations to argue that magnetically saturated BHs release small scale magnetic eruptions leading to the formation of orbiting NIR features, a possible mechanism to explain GRAVITY-observed flares. These papers find that the observed hotspots orbit faster than the simulated NIR features, hinting at super-Keplerian motions (e.g., [Matsumoto et al. 2020](#)). Although these studies restrict their scope to reconnection features in the disk, possible NIR flare models do not yet preclude outflowing features. Outflowing magnetic reconnection zones at wind or jet boundaries, when viewed in projection (e.g., [Ball et al. 2020](#); [Nathanail et al. 2020](#); [Ripperda et al. 2020](#)), could appear to move as the observed hotspots, despite the apparent absence of a well-collimated outflow in Sgr A* (though the size constraints of the central sub-mm source might allow for a jet; e.g., see [Markoff et al. 2007](#); [Issaoun et al. 2019](#)). The highly anticipated results of the Event Horizon Telescope ([Doeleman et al. 2008](#); [EHTC et al. 2019a](#)) observations of Sgr A* promise to reveal much more about the horizon-scale structure and add to the plethora of observational data. Despite the recent advances made in modelling flares, no 3D high resolution GRMHD simulation has yet tackled the inconsistency of Sgr A*'s NIR/X-ray flare flux distribution slopes raised in [Dibi et al. \(2016\)](#) and whether turbulence-driven non-thermal activity explains the overall behaviour of NIR and X-ray flares.

To address these questions, we employ the state-of-the-art GPU-accelerated GRMHD code H-AMR ([Liska et al. 2019](#)) to simulate BH accretion disks and jets and the GRRT code BHoss ([Younsi et al. 2020](#)) to generate spectra assuming a hybrid thermal+non-thermal electron distribution. For the first time, we evolve fully 3D simulations at higher than previously used resolutions and calculate lightcurves over a significantly long time period to study the role of disk and jet turbulence in determining the observed flux variability. The long lightcurves thus produced also provide a key perspective beyond spectral properties. To that end we extract NIR/X-ray flare statistics from the simulations, providing a view of GRMHD BH disks complementary to other recent theoretical papers that focus on magnetised features to explain the NIR flaring (e.g., [Ball et al. 2020](#); [Dexter et al. 2020a](#); [Gutiérrez et al. 2020](#); [Petersen & Gammie 2020](#); [Porth et al. 2020](#)). For the NIR/X-ray flare statistics, we primarily focus on comparing cumulative flux distributions both in the NIR ([Witzel et al. 2012, 2018](#); [Do et al. 2019](#)) and the X-rays ([Neilsen et al. 2013, 2015](#)), restricting our analysis to the inner accretion flow (within $50 r_g$). We provide a detailed overview of our numerical methods in Sec. 2, present and discuss our results in Sec. 3 and 4, and subsequently, conclude in Sec. 5.

2 METHODOLOGY

2.1 GRMHD simulation setup

H-AMR ([Liska et al. 2018](#); [Chatterjee et al. 2019](#); [Porth et al. 2019](#); [Liska et al. 2019](#)) evolves the GRMHD equations set in a fixed Kerr spacetime, specifically in logarithmic Kerr-Schild (KS) coordinates. H-AMR makes use of advanced techniques such as adaptive

GRMHD parameters					
Model	a	Resolution	r_{in}	r_{max}	r_{out}
		$(N_r \times N_\theta \times N_\varphi)$	[r_g]	[r_g]	[r_g]
All	0.9375	$240 \times 144 \times 256$	12.5	25	1000
GRRT parameters					
Model	FOV	Image	Sgr A* $M_{\text{BH}} \& D_{\text{BH}}$		Inclination
	$[r_g \times r_g]$	resolution	$[M_\odot, \text{kpc}]$		[degrees]
All	50×50	1024×1024	$4.1 \times 10^6, 8.15$		85°
Model	R_{high}	R_{low}	Accretion rate	ϵ_C	
			$[M_\odot \text{ yr}^{-1}]$		
Wa93	10	10	3.69×10^{-8}	0.01	
Sa93	40	10	2.96×10^{-8}	2.5×10^{-4}	

Table 1. Top row: GRMHD parameters common to simulation models used in this work - dimensionless BH spin (a), simulation grid resolution, disk inner radius (r_{in}), disk pressure-maximum radius (r_{max}), and outer grid radius (r_{out}). 2nd row: simulation model names, disk magnetic flux strength, time-averaged dimensionless magnetic flux through the event horizon (see Sec. 3.1 for definition), time-averaged density-weighted volume-averaged MRI quality factors ($Q_{r,\theta,\varphi}$, see Sec. 2.1 for definition), and total simulation time (t_{sim}) in r_g/c . 3rd row: GRRT parameters common to radiative models - observer field of view (FOV), GRRT image resolution in pixels, Sgr A* BH mass and distance used for GRRT calculations, and source inclination angle with respect to observer. Bottom row: radiative model names, R_{high} and R_{low} parameters for the electron temperature prescription (Eqn. (3)), the time-averaged accretion rate, and the electron acceleration efficiency coefficient for the constant power-law injection scheme (see Sec. 2.2.1). We calculate the time-average quantities over a period of ~ 60 hrs.

mesh refinement (AMR), static mesh de-refinement, local adaptive time-stepping and a staggered mesh setup for evolving the magnetic field (see [Liska et al. 2019](#) for more details about these methods, and [Porth et al. 2019](#) for comparisons to results from other current GRMHD codes for a standard BH accretion disk problem). We adopt the geometrical unit convention, taking $G = c = 1$, and normalise our length scale to the gravitational radius $r_g = GM_{\text{BH}}/c^2$. The GRMHD simulation grid is axisymmetric and extends from $r = 1.21r_g$ to $10^3 r_g$. We take the BH spin parameter to be $a = 0.9375$ and therefore, our inner radial boundary is inside the event horizon radius ($r_H = 1.347r_g$). The grid resolution is $N_r \times N_\theta \times N_\varphi \equiv 240 \times 144 \times 240$. We use outflowing radial boundary conditions (BCs), transmissive polar BCs and periodic φ -BCs. We did not make use of AMR in this work.

The accretion disk is set up in the form of the standard [Fishbone & Moncrief \(1976\)](#) hydrostatic torus rotating around the spinning BH (refer to Table 1 for torus and other model specifications). A non-relativistic ideal gas equation of state is assumed: the gas pressure $p_{\text{gas}} = (\gamma_{\text{ad}} - 1)u_g$, where $\gamma_{\text{ad}} = 5/3$ and u_g is the internal energy. We perform two simulations, one that leads to a weak jet (model Wa93) and the other a relatively strong jet (model Sa93). We assume a single poloidal loop in the initial disk magnetic field configuration for both simulations, indicated by the magnetic vector potential (\vec{A}):

$$\text{Wa93 : } A_\phi \propto \begin{cases} \rho - 0.2, & \text{if } \rho > 0.2, \\ 0, & \text{otherwise.} \end{cases} \quad (1)$$

$$\text{Sa93 : } A_\phi \propto \begin{cases} (\rho - 0.05)^2 r^5, & \text{if } \rho > 0.05, \\ 0, & \text{otherwise,} \end{cases} \quad (2)$$

where ρ is the rest-mass gas density in code units. The magnetic field strength in the initial condition is normalised by setting $\max(p_g)/\max(p_B) = 100$, where $p_B = B^2/8\pi$ is the magnetic pressure and B is the magnetic field strength.

The grid resolution is the same for both simulations and is sufficient to resolve the magnetorotational instability (MRI; [Balbus & Hawley 1991](#)) in the disk. We use the standard MRI quality factors $Q_{r,\theta,\phi} = <2\pi v_A^{r,\theta,\phi}>_\rho / <\Delta^{r,\theta,\phi}\Omega>_\rho$ to measure the number of cells resolving the largest MRI wavelength, volume-averaged over the disk (using the gas density ρ as the weight in the average; [Chatterjee et al. 2020](#)). In the definition of Q , v_A^i , Δ^i and Ω are the Alfvén speed in the i -th direction, the corresponding cell size and the fluid angular velocity, respectively. While we adequately resolve the MRI in model Sa93 with Q values above 25 (a minimum of 10 is usually quoted for convergence of disk parameters, see [Hawley et al. 2011; Porth et al. 2019](#)), model Wa93 is only marginally resolved due to weaker magnetic fields in the disk. A brief summary of the simulation details is given in Table 1.

Current grid codes are prone to numerical errors when solving the GRMHD equations for gas density and internal energy within the vacuous jet funnel. These errors are due to gas either being expelled as an outflow or accreted via the BH's gravity, leaving behind a vacuum region that GRMHD codes fail to deal with, hence requiring the use of an ad-hoc density floor model. We set a minimum gas density limit of $\rho_{\min}c^2 \geq \max[p_B/50, 2 \times 10^{-6}c^2(r/r_g)^{-2}]$ and a minimum internal energy limit of $u_{g,\min} \geq \max[p_B/150, 10^{-7}c^2(r/r_g)^{-2\gamma_{\text{ad}}}]$, mass-loading the jet funnel according to the implementation described in [Ressler et al. \(2017\)](#).

2.2 Radiative transfer model

In this section, we describe our model for the electron distribution function, using the general relativistic ray-tracing (GRRT) code BHOSS ([Younsi et al. 2016, 2020](#)) to calculate the corresponding synchrotron emission. We generate multiwavelength images and spectra of both simulations (scaled to the mass and distance of Sgr A*) at a cadence of $5 r_g/c$, accounting for all emission within $50 r_g$ only. We employ a hybrid thermal+non-thermal electron distribution, assuming a relativistic thermal Maxwell-Jüttner distribution for the thermal synchrotron emissivity and absorption (using the prescriptions of [Leung et al. 2011](#)) and two different acceleration models for the non-thermal synchrotron emission. First, we calculate the electron temperature T_e via the [Mościbrodzka et al. \(2016\)](#) prescription based on turbulent heating models that gives us the ion-electron temperature ratio ($R \equiv T_i/T_e$) in the form,

$$R = \frac{R_{\text{low}} + R_{\text{high}}\beta_p^2}{1 + \beta_p^2}, \quad (3)$$

where β_p is the plasma- β , defined as the ratio of the gas and magnetic pressures. The electron temperature then is calculated as:

$$T_e = \frac{m_p p_{\text{gas}}}{\rho k_B R} \quad (4)$$

where m_p and k_B are the proton mass and the Boltzmann constant respectively. We adopt R_{high} and R_{low} values for each simulation model such that we are able produce an average spectrum which resembles the Sgr A*'s sub-mm to NIR spectrum. The specific values of R_{high} and R_{low} are given in Table 1.

Using the electron temperature prescription, we can calculate the thermal synchrotron spectrum from our GRMHD models. Next, we explore two different non-thermal GRRT models of injecting a non-thermal distribution of electrons in magnetised regions and calculate the radiative output of each GRMHD model (see Table 1).

2.2.1 Constant power-law injection: ϵ_C model

First, we consider a simple non-thermal synchrotron model where electrons are accelerated via magnetic dissipation, inspired by the early hybrid thermal+non-thermal model of [Özel et al. \(2000\)](#). Such a treatment for the electron distribution function is similar to several other prior works, e.g., [Markoff et al. \(2001\); Broderick & McKinney \(2010\); Dexter et al. \(2012\); Connors et al. \(2017\)](#). In practice, we inject a population of electrons with an energy density that is a fraction of the available magnetic field energy (e.g., [Broderick & McKinney 2010; Dexter et al. 2012](#)). The co-moving energy density in the non-thermal population (U_{nth}) is given by,

$$U_{\text{nth}} = \int_{\gamma_{\min}}^{\gamma_{\max}} \gamma \frac{dN_{\text{nth}}}{d\gamma} m_e c^2 d\gamma, \quad (5)$$

where we have a power-law distribution $dN_{\text{nth}}/d\gamma \propto \gamma^{-p}$. Here, γ is the electron Lorentz factor, p is the power-law distribution index, and γ_{\max} and γ_{\min} are the maximum and minimum electron Lorentz factors in the distribution, respectively. The injected power-law index is chosen to be $p = 2$, motivated by both observations (e.g., [Nowak et al. 2012](#)) and semi-analytical work (e.g., [Connors et al. 2017](#)). The total thermal energy density is given by,

$$U_{\text{th}} = n_{\text{th}} u_{\text{th}} = n_{\text{th}} f(\Theta_e) \Theta_e m_e c^2, \quad (6)$$

where $n_{\text{th}} = \int_1^\infty N_{0,\text{th}}(dN_{\text{th}}/d\gamma) d\gamma$ is the total thermal electron number density. Here, $\Theta_e (\equiv k_B T_e / m_e c^2)$ is the dimensionless electron temperature with m_e as the electron mass. [Gammie & Popham \(1998\)](#) gives $f(\Theta_e)$ in a simplified form,

$$f(\Theta_e) = \frac{6 + 15\Theta_e}{4 + 5\Theta_e}. \quad (7)$$

This expression for $f(\Theta_e)$ gives us thermal energy density $u_{\text{th}} = (3/2)\Theta_e$ for small Θ_e , i.e., non-relativistic temperatures, and $u_{\text{th}} = 3\Theta_e$ for large relativistic temperatures. The power-law part of distribution is tied to the Maxwellian part via $\gamma_{\min} : \gamma_{\min} = \gamma_{\text{pk}} \approx 1 + u_{\text{th}}/m_e c^2$ (i.e., the peak of the Maxwellian distribution). We set $\gamma_{\max} = \eta_\gamma \gamma_{\min}$. [Markoff et al. \(2001\)](#) found that $\gamma_{\max} \gtrsim 10^5$ is required to explain the [Baganoff et al. \(2001\)](#) X-ray flare, thus motivating an assumed η_γ of 10^4 to achieve large X-ray fluxes in regions with high electron temperatures.

Since we expect efficient particle acceleration to occur in magnetically dominated regions, we use a criterion for the acceleration efficiency that promotes non-thermal activity in regions where the magnetic energy dominates over the rest-mass energy, i.e., where $p_B \gtrsim \rho c^2$ ([Broderick & McKinney 2010](#)). Keeping this in mind, we assume the total non-thermal energy density to be of the form:

$$U_{\text{nth}} = \left(\frac{2\epsilon_C}{1 + \exp(\rho c^2/p_B)} \right) p_B. \quad (8)$$

The above equation, combined with Eqn. (5), gives us the non-thermal electron number density for each grid cell, and captures changes in magnetic energy density that might lead to NIR and X-ray variability, given a constant efficiency coefficient ϵ_C . As Broderick & McKinney (2010) state, Eqn. (8) reduces to $U_{\text{nth}} = \epsilon_C p_B$ in highly magnetised zones. We note that the reduced form of Eqn. (8) is the same as that employed in Dexter et al. (2012), where the authors considered the jet launching region in M87. Particle-in-cell (PIC) simulations provide a more self-consistent explanation of the generation of non-thermal activity by resolving the formation and evolution of plasmoids within current sheets using a fully kinetic framework (e.g., Sironi & Spitkovsky 2014; Guo et al. 2014; Werner et al. 2018; Ball et al. 2018). In the next section, we describe a PIC-motivated radiation model.

2.2.2 Varying power-law injection: ϵ_{PIC} model

In the previous section, we relied on a physically motivated ad-hoc prescription for the acceleration efficiency and a constant power-law index, and remain agnostic about the accelerating process. In the case of magnetic reconnection, PIC simulations suggest that both of these quantities are dependent on the surrounding conditions, such as plasma- β_P and the magnetisation σ_M ($\equiv B^2/4\pi\rho c^2$) (e.g., Werner et al. 2018; Ball et al. 2018, and references therein), especially in the trans-relativistic regime (i.e., $\sigma_M \sim 1$). Current 3D GRMHD simulations lack the resolution required to resolve the small-scale structure of plasmoids, or magnetised blobs of gas, that form as a result of magnetic reconnection in current sheets. Only recently have we seen plasmoid evolution in high resolution 2D GRMHD simulations (Nathanail et al. 2020; Ripperda et al. 2020). While it is conceivable that current sheets may be resolvable using advanced simulation grids such as adaptive meshes, for this study, we rely on current sheets and particle acceleration prescriptions from PIC parameter surveys to generate the variability seen in the X-ray emission of Sgr A*.

We incorporate the non-thermal electron acceleration prescriptions for magnetic reconnection given by Ball et al. (2018). Davelaar et al. (2019) used the same acceleration prescriptions to incorporate non-thermal particles in their simulations of M87. The primary difference in our approach is that whereas Davelaar et al. (2019) employed the use of the relativistic κ -distribution function (Xiao 2006), applying only the power-law index prescription of Ball et al. (2018), we calculate the thermal and non-thermal components of the synchrotron emission separately and account for both PIC-motivated power-law indices and efficiencies. Thus this approach removes two degrees of freedom from our first radiative scheme. We identify current sheets in the disk/sheath as regions with small values of β_P^{-1} (i.e., regions where magnetic fields reconnect and the field strength drops) encapsulated by regions of high β_P^{-1} (e.g., Ripperda et al. 2020). In Ball et al. (2018), the ambient plasma- β_P and magnetisation σ_M (hereafter referred to as $\beta_{P,\text{amb}}$ and $\sigma_{M,\text{amb}}$) are used to parameterise the non-thermal distribution slope and acceleration efficiency. For our simulations, we calculate the ambient values for each cell in a current sheet layer by taking the

average over the nearest 2 cells in each direction as follows:

$$\beta_{P,\text{amb}}^{-1} = \sum_{(i-2,j-2,k-2)}^{(i+2,j+2,k+2)} \beta_P^{-1}(r, \theta, \phi) \quad (9)$$

$$\sigma_{M,\text{amb}} = \sum_{(i-2,j-2,k-2)}^{(i+2,j+2,k+2)} \sigma_M(r, \theta, \phi). \quad (10)$$

Ball et al. (2018) give the power-law electron distribution slope p and the non-thermal acceleration efficiency ϵ_{PIC} in the form:

$$p = A_p + B_p \tanh C_p \beta_{P,\text{amb}}, \quad (11)$$

where $A_p = 1.8 + 0.7/\sqrt{\sigma_{M,\text{amb}}}$, $B_p = 3.7\sigma_{M,\text{amb}}^{-0.19}$, $C_p = 23.4\sigma_{M,\text{amb}}^{0.26}$, and,

$$\epsilon_{\text{PIC}} = \frac{\int_{\gamma_{\text{pk}}}^{\infty} (\gamma - 1) \left[\frac{dN}{d\gamma} - \frac{dN_{\text{th}}(\gamma, \Theta_e)}{d\gamma} \right] d\gamma}{\int_{\gamma_{\text{pk}}}^{\infty} (\gamma - 1) \frac{dN}{d\gamma} d\gamma}. \quad (12)$$

Since the total electron number density is $n_e = n_{\text{th}} + n_{\text{nth}} \equiv \rho/(m_p + m_e)$ ($= n_p$, the total proton number density, due to charge conservation), we can simplify the efficiency as,

$$\epsilon_{\text{PIC}} \equiv \frac{\int_{\gamma_{\text{min}}}^{\gamma_{\text{max}}} (\gamma - 1) \frac{dN_{\text{nth}}}{d\gamma} d\gamma}{\int_{\gamma_{\text{pk}}}^{\infty} (\gamma - 1) \frac{dN_{\text{th}}}{d\gamma} d\gamma + \int_{\gamma_{\text{min}}}^{\gamma_{\text{max}}} (\gamma - 1) \frac{dN_{\text{nth}}}{d\gamma} d\gamma}, \quad (13)$$

where, γ_{pk} is the peak Lorentz factor of the Maxwellian distribution. To simplify the thermal case, we have chosen the minimum limit of the integration over $dN_{\text{th}}/d\gamma$ to be $\gamma = 1$ rather than γ_{pk} , which gives a simpler analytical form for the total thermal energy density shown in Eqn. (6). This assumption for the integral limits for the thermal electron energy density results in a larger population of electrons being accelerated to a power-law in high temperature regions as compared to what we expect from Eqn. (13). However, note that Eqn. (12) is not strictly the same as Eqn. (13) since the numerator in Eqn. (12) is the non-thermal contribution to the electron energy density after the Maxwellian component is removed whereas the numerator in Eqn. (13) includes all electrons with energies $\gamma > \gamma_{\text{pk}}$. Hence, the efficiency should be larger than that predicted by the Ball et al. (2018) prescription. However, both the inaccuracies mentioned above are small and counteract each other, so we expect errors in the output spectrum to be negligible. The Ball et al. (2018) acceleration efficiency prescription is given as follows:

$$\epsilon_{\text{PIC}} = A_\epsilon + B_\epsilon \tanh C_\epsilon \beta_{P,\text{amb}}, \quad (14)$$

where $A_\epsilon = 1 - (4.2\sigma_{M,\text{amb}}^{0.55} + 1)^{-1}$, $B_\epsilon = 0.64\sigma_{M,\text{amb}}^{0.07}$ and $C_\epsilon = -68\sigma_{M,\text{amb}}^{0.13}$. This fit for the efficiency goes to zero for $\sigma_{M,\text{amb}} \ll 1$ (non-relativistic reconnection), and 1 for $\sigma_{M,\text{amb}} \gg 1$ (ultra-relativistic reconnection).

3 RESULTS

3.1 GRMHD evolution

Figure 1 shows 2D cross-sections of the electron number density and temperature as well as the plasma- β of our GRMHD models (Wa93 and Sa93), scaled to the parameters of our radiative models for Sgr A* (see Table 1). The overall jet and disk properties are vastly different between the two models, with the strong field disk model Sa93 displaying wider outflows and lower disk electron number densities and temperatures. The low plasma- β and high

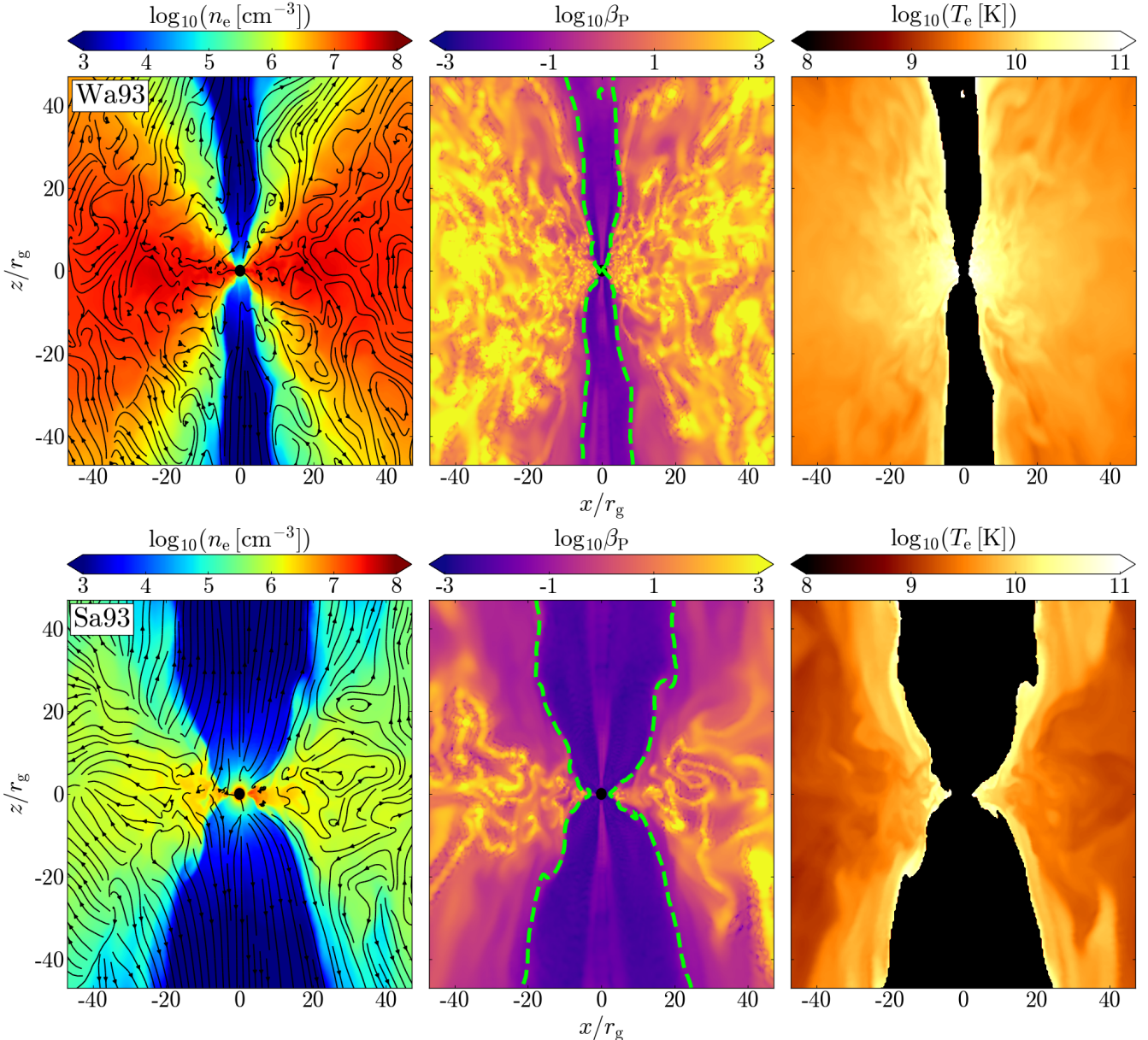


Figure 1. Strongly magnetised disks exhibit wider jets, magnetically dominated winds and lower disk densities and temperatures as compared to their weak disk counterparts. We show x-z cross-sections of the electron number density n_e (with velocity streamlines in black), plasma- β and electron temperature T_e from our GRMHD simulations: (top row) weak field disk model Wa93 and (bottom row) strong field disk model Sa93, scaled to Sgr A* according to Table 1. We also indicate the jet boundary (approximated as magnetisation $\sigma_M = 1$) in green for the plasma- β plots. Further, the jet is cut out (black region) in the T_e plots, since we do not account for the jet spine emission in our radiative scheme. The final time snapshots of each simulation are shown.

temperatures in the Sa93 outflow region suggests that the bulk of the synchrotron emission would originate in the jet sheath, whereas for the weak field disk model Wa93, the disk would produce a dominant fraction of the radiation. This result crucially depends on the electron temperature prescription shown in Sec. 2.2 (also see Fig. 4 in EHTC et al. 2019b). However, given that the non-thermal acceleration efficiency and power-law index is sensitive to the local magnetisation and plasma- β , we expect that regions of low plasma- β , i.e., the jet sheath would dominate the majority of X-ray emission.

Figure 2 shows the time evolution of our simulations, illustrating the horizon accretion rate \dot{M} , the horizon energy accretion rate

\dot{E} , the horizon outflow efficiency (i.e., the ratio of the outflow power P_{out} and the accretion power $\dot{M}c^2$), the horizon dimensionless magnetic flux $\phi_{\text{BH}} = \Phi_{\text{BH}}/(\dot{M}r_g c^2)^{1/2}$ and the disk barycentric radius r_{disk} , defined as:

$$\dot{M} = - \iint \rho u^r \sqrt{-g} d\theta d\varphi, \quad (15)$$

$$\dot{E} = \iint T_t^r \sqrt{-g} d\theta d\varphi, \quad (16)$$

$$P_{\text{out}} = \dot{M}c^2 - \dot{E}, \quad (17)$$

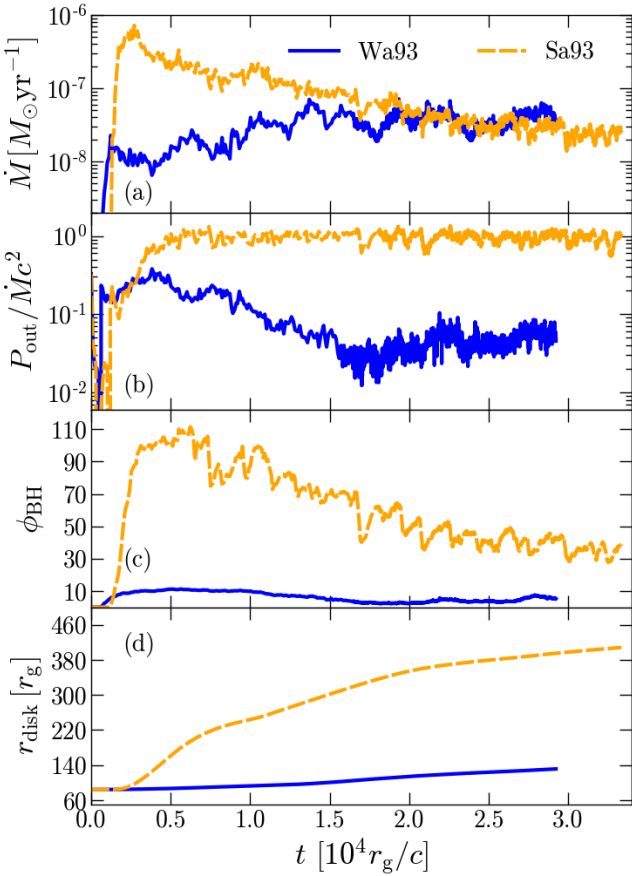


Figure 2. Time evolution of several simulation physical parameters, comparing between the weak field Wa93 and the strong field Sa93 models. Panels show the (a) mass accretion rate \dot{M} in $M_\odot \text{ yr}^{-1}$, (b) dimensionless outflow power efficiency $P_{\text{out}}/\dot{M}c^2$, (c) dimensionless magnetic flux ϕ_{BH} , and (d) barycentric radius r_{disk} in units of r_g . We measure all quantities at the event horizon. Section 3.1 lists the definition of each quantity.

$$\Phi_{\text{BH}} = \frac{1}{2} \iint |B'| \sqrt{-g} d\theta d\varphi, \quad (18)$$

$$r_{\text{disk}} = \frac{\iint r \rho \sqrt{-g} d\theta d\varphi}{\iint \rho \sqrt{-g} d\theta d\varphi}. \quad (19)$$

where T'_r , u' , B' and $g \equiv |g_{\mu\nu}|$ are the total radial energy flux, radial velocity, radial magnetic field and the metric determinant respectively (standard definitions from e.g., Porth et al. 2019; Chatterjee et al. 2020). The weak field model, Wa93, produces a jet with an average efficiency of $P_{\text{out}}/\dot{M}c^2 \lesssim 6\%$ while the strong field model (Sa93) jet attains an efficiency of almost 100%. Jet efficiencies $\gtrsim 100\%$ are known to occur when the magnetic pressure around the BH becomes sufficiently dominant to obstruct gas from accreting (e.g., Narayan et al. 2003; Tchekhovskoy et al. 2011), leading to a magnetically arrested disk (MAD) state. Indeed, as shown in Dexter et al. (2020a) and Porth et al. (2020), MAD conditions lead to magnetic eruptions where magnetised low density bunches of field lines (i.e., flux tubes) escape from the BH's event horizon and interact with the surrounding accretion material via shearing instabilities, heating up electrons and causing NIR flaring events (Dexter et al. 2020a).

While neither simulation develops a MAD-like disk, Sa93 displays a significantly higher jet power as well as horizon magnetic

flux, which considerably changes disk-jet dynamics close to the BH, especially with respect to disk turbulence. Stronger outflows lead to a higher rate of momentum transport outwards and hence cause the disk to viscously spread out as illustrated by the increasing value of r_{disk} over time in the case of Sa93. One important question remains for MADs or even strong field disks in the context of Sgr A*: these types of disks always produce powerful jets that seem to be absent in Sgr A*. From the ongoing EHT observations of Sgr A*, we will hopefully be able to place much better constraints on the size of the source as well as the structure of the horizon-scale flow, which will prove crucial to settling the question of jets from Sgr A*. Our goal is to understand the effect of disk or jet turbulence on variability in a quasi-stable disk whereas for MADs, the presence of magnetic eruptions distort the inner structure of the accretion flow.

3.2 Multiwavelength spectrum of Sgr A*: observations and GRRT modelling

We generate spectra for each of our hybrid thermal+non-thermal models assuming the BH mass and distance of Sgr A* (see Table 1: GRRT parameters). From Fig. 2(a), we see that the accretion rate for each model at first increases, marking the start of accretion from the torus, and then slowly decreases and finally settles at a time $t \simeq 1.5 \times 10^4 r_g/c$ for model Wa93 and at $t \simeq 2 \times 10^4 r_g/c$ for model Sa93. We choose a time segment spanning in excess of 60 hours for each simulation. The source inclination angle with respect to the observer is taken to be 85° in accordance with previous Sgr A* models (e.g., Markoff et al. 2007; Mościbrodzka et al. 2009; Shcherbakov et al. 2012; Drappeau et al. 2013; Connors et al. 2017). Sgr A*'s inclination angle is still an open question with several other works employing smaller inclinations (e.g., Dexter et al. 2010; Mościbrodzka & Falcke 2013; Chael et al. 2017; Davelaar et al. 2018; Gravity Collaboration et al. 2020b). The source azimuthal angle with respect to the observer is taken to be 0° as the BH disk-jet system is roughly axisymmetric (this quantity only becomes important for misaligned BH disks, see Chatterjee et al. 2020). The field-of-view (FOV) for the GRRT imaging is $50 r_g \times 50 r_g$ with an image resolution of 1024×1024 pixels. Figure 3 shows the multiwavelength spectrum for each radiative model: the mean spectrum along with 1σ deviations, and the maximum X-ray flare spectrum. The mass accretion rate for each model is chosen to match the observed sub-mm fluxes: $3.69 \times 10^{-8} M_\odot \text{ yr}^{-1}$ for Wa93 and $2.12 \times 10^{-8} M_\odot \text{ yr}^{-1}$ for Sa93. These accretion rates lie well within the range of inferred values for Sgr A* (Bower et al. 2003; Marrone et al. 2007). The choice of R_{high} and R_{low} is made such that mean spectrum roughly fits the 230 GHz flux, while not overproducing the NIR emission. We note that in the case of Wa93- ϵ_{PIC} (Fig. 3b), lower values of R_{low} can be used to preferentially heat the electrons in low plasma- β_P regions, such as the jet sheath. However, for this work, to keep the models comparable, we choose the same value of R_{low} for each model, varying only R_{high} and therefore, the electron temperature in the disk. The change in spectral index at frequencies above 10^{17} Hz occurs due to synchrotron cooling, with the turnover frequency set by equating the local advective and synchrotron cooling timescales.

During periods of flaring, the non-thermal contribution to the NIR flux increases and affects the NIR slope in the spectrum of 3 models (Fig. 3a,b,d), while in the case of Sa93- ϵ_{C} , the thermal synchrotron emission dominates the NIR emission. None of the models are able to simultaneously reproduce the NIR GRAVITY flux and the Hornstein et al. (2007) slope, while the brightest X-ray flare

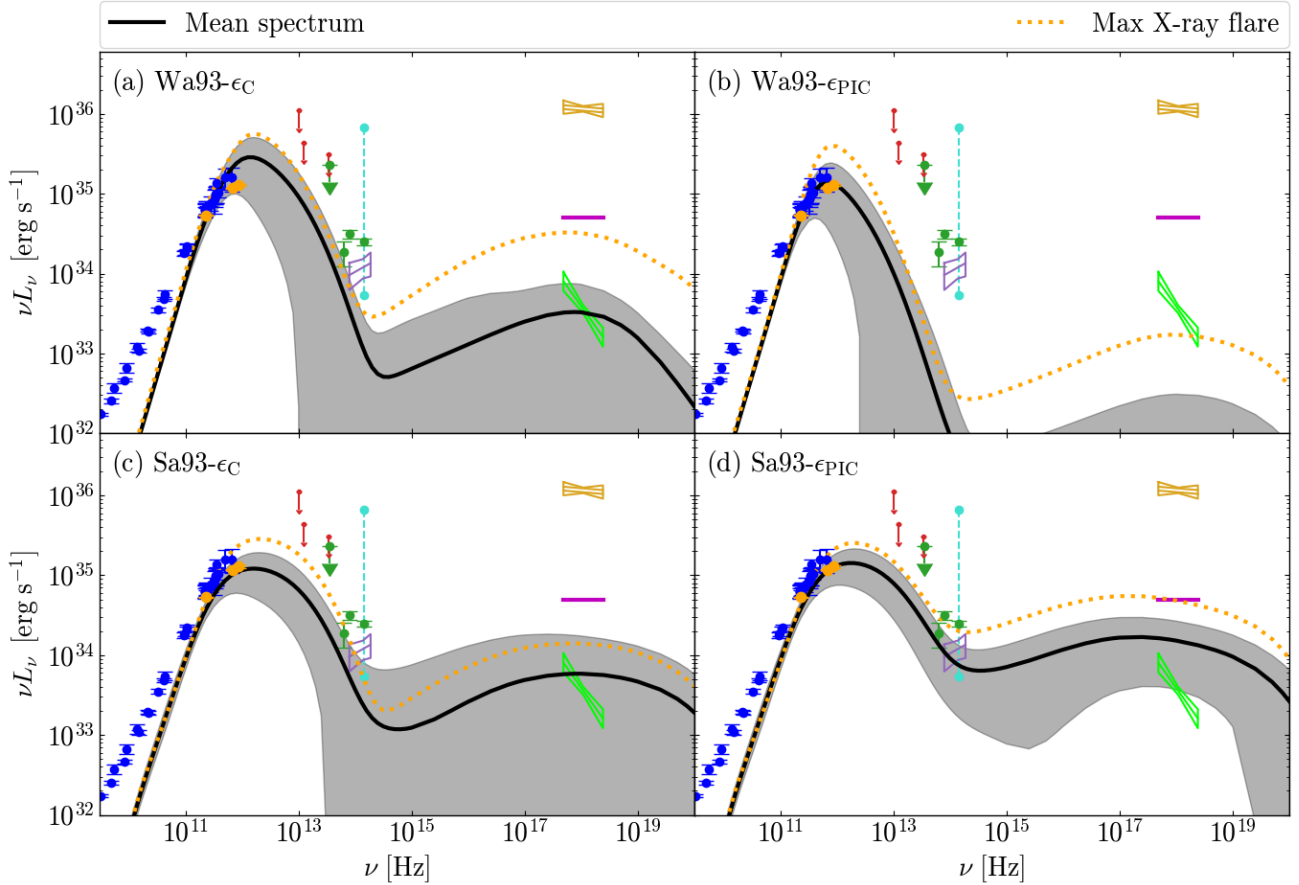


Figure 3. Multiwavelength spectra for each radiative model: (a) Wa93- ϵ_C - weak field simulation + constant power-law injection non-thermal model, (b) Wa93- ϵ_{PIC} - weak field simulation + varying power-law injection non-thermal model, (c) Sa93- ϵ_C - strong field simulation + constant power-law injection non-thermal model and (d) Sa93- ϵ_{PIC} - strong field simulation + varying power-law injection non-thermal model. We show the mean spectrum over the considered time segment (black solid line) along with 1σ standard deviations from mean (in grey), and the spectrum for the simulation snapshot with the brightest X-ray flare (orange dotted line). We include radio and sub-mm data points quoted in Connors et al. (2017, blue circles), compiling historical data from Zylka et al. (1995); Serabyn et al. (1997); Falcke et al. (1998); Zhao et al. (2001); Nord et al. (2004); Roy & Pramesh Rao (2004); An et al. (2005); Lu et al. (2011); Brinkerink et al. (2015); Bower et al. (2015). We also include recent sub-mm observations at 233, 678 and 870 GHz from Bower et al. (2019, orange circles), with mid-infrared datapoints from Schödel et al. (2011, green circles and an arrow) and infrared upper bounds from Melia & Falcke (2001, red arrows). Furthermore, we combined the Gravity Collaboration et al. (2020a) median flux 1.1 ± 0.3 mJy at $2.2 \mu\text{m}$ with the spectral index $\alpha_\nu = -0.6 \pm 0.2$ measured over $1.6 - 3.8 \mu\text{m}$ from Hornstein et al. (2007) to create the purple bowtie. We show the maximum and minimum dereddened fluxes (59.6 and 0.48 mJy, respectively) at $2.2 \mu\text{m}$ from Do et al. (2019, cyan circles) to guide our NIR flare spectra. For the X-ray quiescent spectrum (lime bowtie), we take the 2-8 keV luminosity of $L_X = (3.6 \pm 0.4) \times 10^{33}$ erg s $^{-1}$ and photon index $\Gamma = 3.0 \pm 0.2$ from Nowak et al. (2012), while for the flaring state, we show the average flare spectrum with $L_X \simeq 5 \times 10^{34}$ erg s $^{-1}$ with $\Gamma = 2$ from Neilsen et al. (2015, magenta line). We also show the brightest X-ray flare detected to date: a double-peaked flare with $L_X = (12.26^{+0.28}_{-0.27}, 10.97^{+0.28}_{-0.27}) \times 10^{35}$ erg s $^{-1}$ and $\Gamma = 2.06 \pm 0.1$ from Haggard et al. (2019, golden bowtie). There is a significant difference in synchrotron emission from the considered hybrid thermal+non-thermal electron energy distributions, particularly in variability when comparing the weak and strong field models. None of the models achieve the high NIR and X-ray luminosities seen in Do et al. (2019) and Haggard et al. (2019), respectively.

spectrum of Wa93- ϵ_C displays a similar slope, but fails to produce the required NIR flux. The weak field radiative models produce low X-ray fluxes while the mean spectrum for the strong field models overproduce the quiescent X-ray limits. Additionally, the extent of the 1σ standard deviation region about the mean spectrum (in grey) indicates that the variability in the spectra for the strong field models is quite low. This suggests that strong magnetic fields near the BH lead to the continuous formation of highly magnetised current sheets in the inner accretion disk, as evidenced by the small value of ϵ_C required for the acceleration efficiency such that we do not overproduce the X-ray emission. Since the inner disk in Sa93

is highly magnetised, we see higher X-ray emission overall with model Sa93- ϵ_{PIC} achieving the brightest flare with an X-ray luminosity exceeding the average flare luminosity. Among the models that produce X-ray luminosities above quiescence, Wa93- ϵ_C produces the largest relative change in X-ray luminosity between the mean and brightest flare spectrum with a difference of over an order of magnitude. It is further encouraging to note that in the case of the PIC-motivated radiation models, the change in power-law index p of the non-thermal distribution occurs at $\nu \sim 10^{17}$ Hz due to synchrotron cooling and hence, the X-ray power-law index during the brightest flares is $p + 1 \sim 3$, consistent with the photon indices

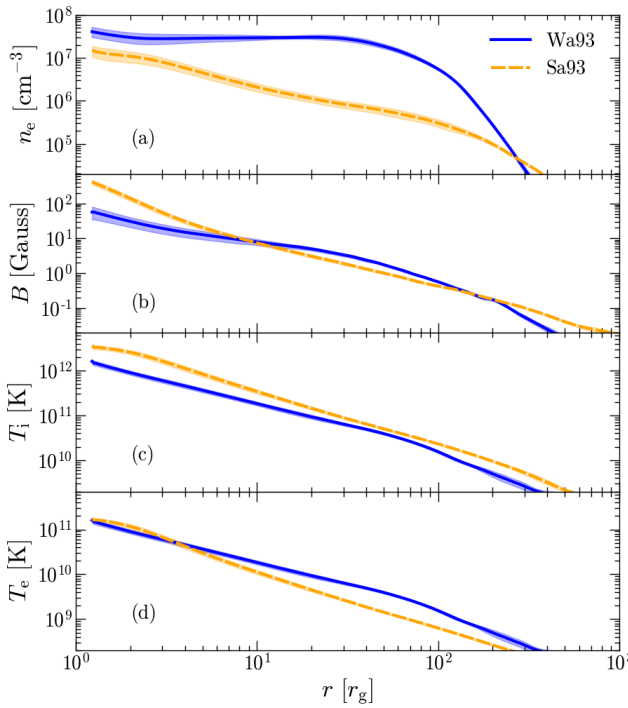


Figure 4. Radial dependencies of the disk-averaged quantities: (a) electron number density n_e in cm^{-3} , (b) the magnetic field strength B in Gauss, (c) the ion (or proton) temperature T_i and (d) the electron temperature T_e in Kelvin, when scaled to the mass and accretion rate of Sgr A*. We calculate T_e using eqns. (3) and (4) as per quoted values in Table 1. Wa93 contains a larger electron concentration in the disk and exhibits a near constant radial profile, while Sa93 displays a steeper power-law profile due to stronger disk turbulence. The magnetic field strengths are similar between the two models, apart from the inner $5 r_g$ where Sa93 displays field strengths larger by factors of 5-8. Stronger turbulence leads to slightly higher ion temperatures in the inner disk of Sa93, whereas the electron temperatures in the two models behave very similarly, exhibiting an approximate r^{-1} profile.

measured by Nowak et al. (2012) and Haggard et al. (2019). This result verifies the claim that simultaneous NIR and X-ray flares are perhaps related via a broken power-law distribution (e.g., Dodds-Eden et al. 2010; Dibi et al. 2014; Ponti et al. 2017), and strongly points towards a non-thermal origin for Sgr A* flaring.

3.3 Disk-averaged profiles

Figure 4 shows the disk-averaged values of the electron number density n_e in cm^{-3} , magnetic field strength B in Gauss, and the ion and electron temperatures, T_i and T_e respectively, in Kelvin for both Wa93 and Sa93 simulations, when scaled to the BH mass of Sgr A* and the aforementioned accretion rates. The disk-averaging for a parameter $q \in (\rho, B, T_i, T_e)$ is calculated in the form,

$$\langle q \rangle = \frac{\iint q \rho \sqrt{-g} d\theta d\varphi}{\iint \rho \sqrt{-g} d\theta d\varphi} \quad (20)$$

similar to the evaluation of the barycentric radius r_{disk} in the previous section. As mentioned in the previous section, from Fig. 2(d), we see that the strong field Sa93 disk grows larger over time and hence, becomes more diffused, leading to lower n_e values in the disk as compared to the weak field model Wa93 (Fig. 4a). Even though the Sa93 ion temperature is higher, the electron temperatures from the two simulations are roughly similar in the disk since

the R_{high} parameter for Sa93 is 4 times as large as for Wa93. In the next section, we study the variable properties of the observed lightcurves that are the outcome of disk turbulence and magnetic reconnection in the current sheets.

4 VARIABILITY IN LIGHTCURVES

In this section, we perform timing analysis of the radiative models studied in the previous section. We consider three specific wave bands and compare our results with three corresponding observational papers: 230 GHz - Dexter et al. (2014), 2.12 μm - Do et al. (2019) and 2-8 keV - Neilsen et al. (2015). Figure 5 shows the lightcurves in each of the three bands, for each model (Table 1). For comparison with the observational data, we construct the fractional root-mean-square (rms) normalised power spectral density (PSD) curves for each set of lightcurves (Fig. 6) and cumulative distribution functions (CDFs) for the 2.2 μm and X-ray lightcurves (Figs. 7, 8 and 9). To reduce noise at high frequencies in the PSDs, we re-bin logarithmically and average over frequency bins. In the following subsections, we look at each waveband in turn and discuss the lightcurves, PSDs and CDFs for each model.

4.1 Sub-millimeter: 230 GHz

Figure 5(a) shows that the weak field model 230 GHz lightcurves- $\text{Wa93-}\epsilon_{\text{C}}$ and $\text{Wa93-}\epsilon_{\text{PIC}}$ are similar to each other on average and show an increase of a factor $\lesssim 2$ in the flux at late times, largely following the variations in the accretion rate. The similarity in lightcurves between the radiative models is more stronger for the strong field disk cases, $\text{Sa93-}\epsilon_{\text{C}}$ and $\text{Sa93-}\epsilon_{\text{PIC}}$: the 230 GHz lightcurves lie almost on top of each other. This suggests that the bulk of the 230 GHz emission is being produced in the same region for each GRMHD model, as is expected since the emission is thermal in nature and there is only one electron temperature distribution for each simulation model. The accretion rate is scaled such that the 230 GHz flux is the same for all models. However, as seen from the average spectrum in Fig. 3(a) vs (b), there is a noticeable addition to the terahertz flux in the case of model $\text{Wa93-}\epsilon_{\text{C}}$ due to the presence of a higher percentage of thermal electrons in the jet sheath in comparison to $\text{Wa93-}\epsilon_{\text{PIC}}$. This is due to the acceleration prescription used in $\text{Wa93-}\epsilon_{\text{C}}$ where magnetic energy is transferred to the non-thermal energy density. Hence, the regions closest to the BH (where the magnetic field is the strongest) is favoured as the region of electron acceleration as opposed to the jet sheath. This is not the case for the strong field radiative models: the radio-to-infrared spectra are almost similar.

Figure 6(a) shows the 230 GHz PSD as a function of the Fourier sampling frequency (ν_F) for each model. At high frequencies, all models behave like red noise with a power-law dependence on ν_F of ≈ -2 . The 230 GHz rms% value of all the models (Table 2) matches the accretion rate rms% as well as the observed 20-30% variation seen in the sub-mm lightcurves of Sgr A* (e.g., Zhao et al. 2003; Marrone et al. 2008; Dexter et al. 2014). For the weak field models, the red-to-white turnover occurs at frequencies close to 0.001 min^{-1} pointing to a characteristic variability timescale (τ_{rms}) of the order of tens of hours. For the strong field model, the turnover appears to occur at slightly higher frequencies ($\sim 0.003 \text{ min}^{-1}$), which is close to measured variability timescale of Sgr A* (≈ 8 hours of Sgr A*; Dexter et al. 2014). Currently, the lowest frequency bins in the averaged PSDs contain a single datapoint,

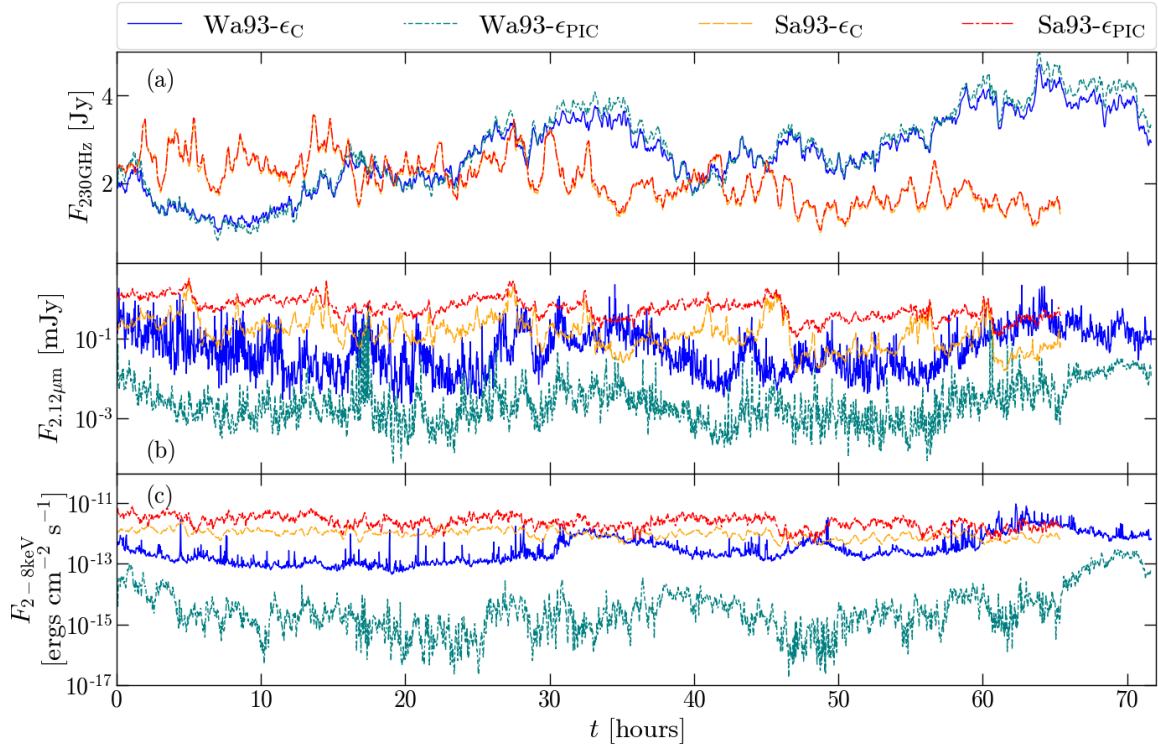


Figure 5. GRRT lightcurves for each model at 3 wavebands in the standard units used in the literature: (a) 230 GHz in Jansky [Jy], (b) near-infrared (NIR at $2.12\ \mu\text{m}$) in milli-Jansky [mJy] and (c) X-rays (integrated over 2-8 keV) in $\text{erg cm}^{-2}\ \text{s}^{-1}$. The 230 GHz lightcurves largely follow the corresponding model accretion rate over time, and therefore, lightcurves from a particular simulation model (Wa93 or Sa93) behave in a similar fashion. The NIR lightcurves for the Sa93 radiative models are also roughly correlated since thermal synchrotron emission dominates the NIR emission. For $\text{Wa93-}\epsilon_{\text{C}}$, both thermal and non-thermal electrons contribute to the NIR emission, whereas there is hardly any significant non-thermal contribution in $\text{Wa93-}\epsilon_{\text{PIC}}$. The lack of non-thermal electrons in $\text{Wa93-}\epsilon_{\text{PIC}}$ results in extremely low X-ray fluxes while $\text{Wa93-}\epsilon_{\text{C}}$ exhibits intermittent flares. The X-ray lightcurve for $\text{Sa93-}\epsilon_{\text{PIC}}$ looks more variable with relatively larger changes in flux as compared to $\text{Sa93-}\epsilon_{\text{C}}$.

and hence the standard error for each bin is equal to the power itself, which would introduce large error-bars for the best-fit value of variability timescale. Capturing the white noise regime properly is essential for accurately fitting for the variability timescale, and hence, requires a lightcurve that is at least one order of magnitude longer than that calculated in this study.

4.2 Near-infrared: $2.12\ \mu\text{m}$

Figure 5(b), 6(b) and 7 show the lightcurves, power spectra and the cumulative distribution functions at $2.12\ \mu\text{m}$ (NIR) wavelength. We see that the $\text{Wa93-}\epsilon_{\text{C}}$ and $\text{Sa93-}\epsilon_{\text{PIC}}$ NIR lightcurves display, on average, higher fluxes than that for $\text{Wa93-}\epsilon_{\text{PIC}}$ and $\text{Sa93-}\epsilon_{\text{C}}$, respectively. The PSDs for the strong field models are similar and display a power-law slope close to ν_{F}^{-2} . The weak field model PSDs are strikingly different from the strong field cases, exhibiting flatter slopes at high Fourier frequencies. This is consistent with variability in extremely low fluxes being uncorrelated events, in the form of multiple weakly magnetised current sheets in the accretion flow.

The weak field NIR lightcurves display high rms variability with rms% values $\sim 150\%$ for $\text{Wa93-}\epsilon_{\text{C}}$ and 300% for $\text{Wa93-}\epsilon_{\text{PIC}}$ (Table 2), which stems from the rapidly fluctuating non-thermal component. These values are close to the observed NIR rms amplitude ($\gtrsim 170\%$; Witzel et al. 2018). This can be seen from Fig. 5(b)

Model	rms%			
	230 GHz	$2.12\ \mu\text{m}$	2-8 keV	\dot{M}
$\text{Wa93-}\epsilon_{\text{C}}$	31.58	158.70	143.94	24.5
$\text{Wa93-}\epsilon_{\text{PIC}}$	34.76	304.59	275.63	24.5
$\text{Sa93-}\epsilon_{\text{C}}$	25.33	123.66	33.05	23.8
$\text{Sa93-}\epsilon_{\text{PIC}}$	24.43	61.33	45.04	23.8

Table 2. Particle acceleration results in highly variable NIR and X-ray emission for Sgr A*. We show the fractional rms amplitude (rms%) from the power spectra (Fig. 6) of the 230 GHz, $2.12\ \mu\text{m}$ and 2-8 keV Sgr A* lightcurves as well as the accretion rate for each model (Table 1). While the 230 GHz rms% values are uniform across all models, there is a large range of rms% in both the NIR and the X-ray lightcurves.

as the flux from both models (blue solid line for $\text{Wa93-}\epsilon_{\text{C}}$ and teal dash-dotted line for $\text{Wa93-}\epsilon_{\text{PIC}}$) vary by a factor of 100 over the lightcurve duration. One way to decrease the rms% is to account for synchrotron self-Compton (SSC) upscattering of thermal synchrotron photons as this process might contribute significantly during low flux states (e.g., as seen from Fig. 2 in Mościbrodzka et al. 2009, also see Eckart et al. 2004). The importance of low-level flux

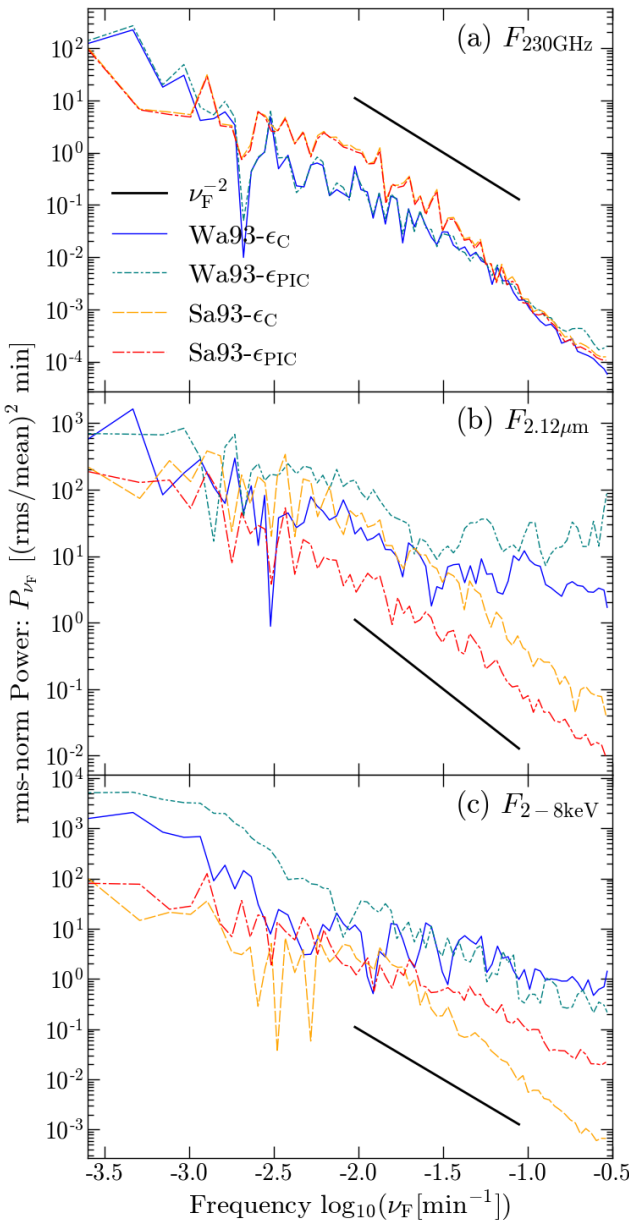


Figure 6. Fractional root-mean-square (rms) normalised power spectral density (PSD; P_{ν_F}) plots for each radiative model at (a) 230 GHz, (b) $2.12 \mu m$ and (c) 2-8 keV integrated X-ray flux. The x-axis frequency ν_F corresponds to the inverse of timescales. We also show a black line in each plot representing ν_F^{-2} dependence, a characteristic of red noise turbulence. At high frequencies, while the 230 GHz PSDs behave similar to red noise, the NIR and X-ray PSDs exhibit shallower profiles at high frequencies, closer to ν_F^{-1} and even frequency-independent behaviour. The absence of pronounced white noise at low frequencies indicates that we are unable to capture long-timescale variability due to the short length of our lightcurves.

events in the overall flux distribution is illustrated more clearly in the CDFs, shown in Fig. 7.

The CDF ($N_{\geq F}$) is defined as the fraction of the total number of

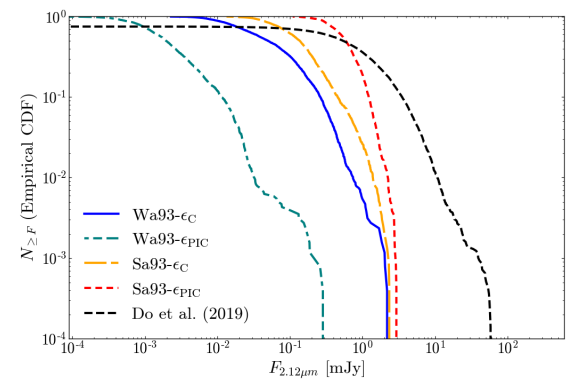


Figure 7. Standard GRMHD models are unable to reproduce the NIR flux distribution. We show the $2.12 \mu m$ (near-infrared; NIR) flux cumulative distribution functions (CDFs) for each radiative model along with the Do et al. (2019) measured CDF for Sgr A*. While none of the models provide a satisfactory match to the observed CDF, the strong field models, Sa93-\epsilon_C and Sa93-\epsilon_{PIC}, display similar low-to-high flux transition but not enough high flux events. Both weak field models fail to produce sufficient quiescent emission compared to the data, but display a similar shape for the power-law tail. This pronounced power-law tail suggests a highly variable NIR flux, which is also reflected from the high NIR rms% values in Table 2.

GRRT snapshots (N_{net}) where the emitted flux at a given frequency exceed or equals a certain threshold flux F ,

$$N_{\geq F} = \frac{1}{N_{\text{net}}} \sum_{i=1}^{N_{\text{net}}} \text{if}(F_i \geq F), \quad (21)$$

where F_i are the fluxes for each GRRT time snapshot, and $N_{\text{net}} = 2555$ and 2332 for the weak field and strong field models, respectively. In Fig. 7, we see that the strong field models display the same quiescent flux level (black dashed line) from Do et al. (2019), but does not show enough high flux events. This can be explained via the strong field spectra (Fig. 3c,d), where we see that the NIR spectrum shows less variability compared to the weak field models, and there are not enough high level flux events to skew the CDF towards a power-law. For the weak field models, the situation is entirely different as there are too few moderate level flux events and hence, the CDF transitions to a steeper power-law at a smaller flux threshold than for the observed CDF. Here, SSC can contribute to the moderate and low flux levels and skew the CDF transition flux threshold to a higher value. Further, more efficient electron acceleration must occur to explain the high flux excursions as seen in Do et al. (2019). A log-normal + power-law-tail distribution describes the weak field model CDFs better than a log-normal distribution, consistent with the results of Dodds-Eden et al. (2010); Petersen & Gammie (2020).

4.3 X-rays: 2-8 keV

Figures 5(c) and 6(c) show the 2-8 keV lightcurves given in units of $\text{erg cm}^{-2} \text{ s}^{-1}$ and the corresponding power spectra for each model, respectively. From Sec. 3.2, we see that model Wa93-\epsilon_C displays a mean spectrum over the considered time duration of ~ 70 hours that coincides with the total quiescent X-ray emission of Sgr A* from Nowak et al. (2012). The lack of any variability in the quiescent spectrum over two decades of observations strongly favours the origin to be thermal bremsstrahlung emission from close to Bondi

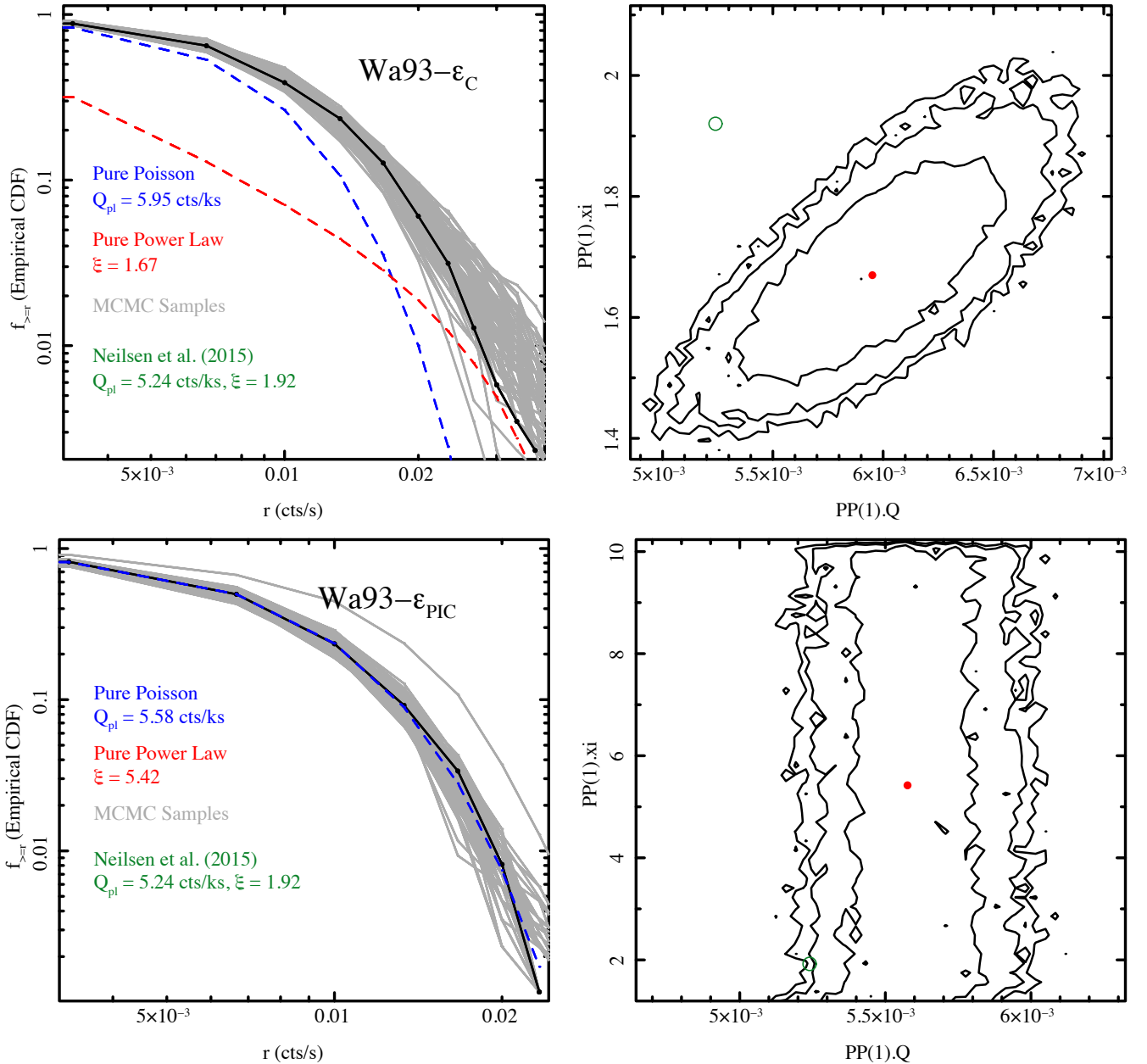


Figure 8. We show cumulative distribution functions ($f_{\geq r}$) as a function of the flux count rate (r) for the X-ray 2–8 keV lightcurve (panels a and c) constructed from the the weak field radiative models: (a, b) $\text{Wa93-}\epsilon_{\text{C}}$ and (c, d) $\text{Wa93-}\epsilon_{\text{PIC}}$. The radiative model CDF (black line) is fitted with a Poissonian component (blue-dashed) to represent the quiescent flux distribution and a variable process in the form of a power-law (red-dashed), as indicated by the best-fit values of the Poisson rate Q_{pl} and the power-law index ξ (see Sec. 4.3). In order to directly compare to Sgr A* X-ray CDFs from Neilsen et al. (2015), we add a quiescent background count rate to the flux distribution. The grey lines in panels (a,c) are the results of Markov Chain Monte Carlo simulations from the joint probability distribution of Q_{pl} and ξ . We also show probability contour plots that illustrate the correlation between parameters Q_{pl} and ξ (panels b and d), with contours corresponding to 68%, 90% and 95% confidence levels. The red circle indicates the most probable values for the parameters, while the green circle shows the Neilsen et al. (2015) fit values. $\text{Wa93-}\epsilon_{\text{C}}$ provides reasonable values for the parameter fits to that seen for Sgr A*. Since $\text{Wa93-}\epsilon_{\text{PIC}}$ does not display significant X-ray flux excursions, the quiescent background dominates throughout with a statistically insignificant fit for ξ .

scales (e.g., Quataert 2002), which is supported by the resolve extension beyond *Chandra*'s PSF (Wang et al. 2013). The high mean emission from this model is the outcome of an increase in the accretion rate over the time segment, that also drives a steady increase in the 230 GHz flux (Fig. 5a: blue solid line). On the other hand, $\text{Wa93-}\epsilon_{\text{PIC}}$ produces an X-ray lightcurve that is considerably dimmer, even failing to reproduce the expected non-thermal contribution to the quiescent emission. The weak field X-ray lightcurves are less vari-

able as compared to their NIR counterparts, with a rms amplitude of $\sim 144\%$ (for $\text{Wa93-}\epsilon_{\text{C}}$; Table 2) and $\sim 275\%$ (for $\text{Wa93-}\epsilon_{\text{PIC}}$). These values are within an order of magnitude of the observed rms amplitude in X-rays ($\sim 100 - 1000$) for Sgr A*. The strong field models exhibit similar lightcurves to each other, with $\text{Sa93-}\epsilon_{\text{PIC}}$ displaying higher flux levels than $\text{Sa93-}\epsilon_{\text{C}}$ almost throughout the chosen time duration. The strong field model PSDs look similar with comparable rms%, as the origin of the emission is the same in the two

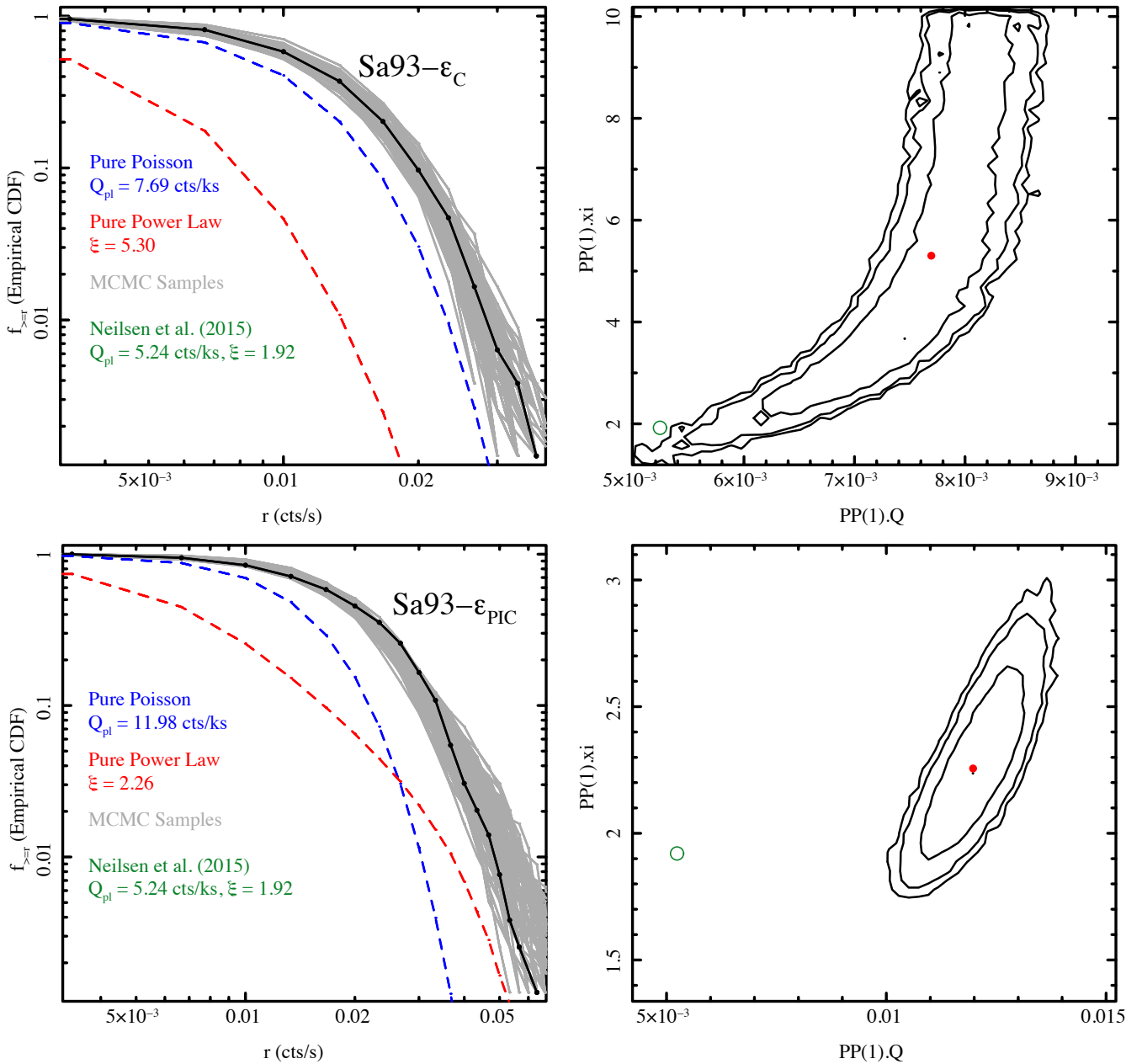


Figure 9. Same as Fig. 8, but for strong field radiative models, $\text{Sa93-}\epsilon_{\text{C}}$ and $\text{Sa93-}\epsilon_{\text{PIC}}$. The CDF of $\text{Sa93-}\epsilon_{\text{C}}$ is well explained with the Poissonian component, while for $\text{Sa93-}\epsilon_{\text{PIC}}$, the CDF displays a much higher rate Q_{pl} for the Poisson process than all other models as well as a statistically significant power-law tail.

radiative models: the low plasma- β jet sheath. The small difference in the variability between $\text{Sa93-}\epsilon_{\text{C}}$ and $\text{Sa93-}\epsilon_{\text{PIC}}$ is more noticeable in their flux distributions, which we calculate next.

To directly compare our X-ray CDFs to those obtained from the *Chandra* 3 Ms Sgr A* 2012 X-ray Visionary Project, we closely follow the methodology given in Neilsen et al. (2015). We process our GRRT X-ray lightcurves using the same tools used to analyse observed *Chandra* lightcurves. To this effect, we use the Interactive Spectral Interpretation System (ISIS; Houck & Denicola 2000) to fold our model lightcurves with High Energy Transmission Grating Spectrometer (HETGS) *Chandra* Sgr A* responses from Nowak et al. (2012). Following Sec. 4.1 in Nowak et al. (2012), we include interstellar absorption with the model TBnew (Wilms et al. 2000) with Verner et al. (1996) cross-sections, assuming the hy-

drogen column density $N_{\text{H}} = 14.3 \times 10^{22} \text{ cm}^{-2}$. We then calculate the predicted 2-8 keV count rates. We derive the zeroth order count rates as well as the first order count rates for both HETG grating sets, the medium-energy gratings (MEG) and the high-energy gratings (HEG). We reduce the simulated zeroth order count rates for photon pileup assuming the same scaling as in Neilsen et al. (2015) since this effect may be as strong as 10-15% for the highest count rates. We then combine the zeroth and first order count rates to calculate the final intrinsic lightcurve (i.e., this does not include the quiescent emission). For the CDF calculation, we assume a quiescent background X-ray count rate of 5.24 counts/ks to represent the bremsstrahlung contribution from larger scales, adding Poisson noise and interpolating the processed lightcurve onto 300 s bins as done in Neilsen et al. (2015).

Figures 8 and 9 show the obtained CDFs and the 2D probability contour plots for the weak field and strong field models. We represent each radiative model CDF (black lines in the figures) as a combination of a Poisson process (blue dashed) with rate Q_{pl} to characterise the low flux level quiescent emission, and a power-law tail (red dashed) with index ξ for the flare emission. Following Neilsen et al. (2015), we then run Markov Chain Monte Carlo simulations (grey lines) to find maximum likelihood fits for Q_{pl} and ξ and compare to the best fit values obtained from *Chandra* observations, given in Neilsen et al. (2015): $Q_{\text{pl,bf}} = (5.24 \pm 0.08)$ counts/ks and $\xi_{\text{bf}} = 1.92^{+0.03}_{-0.02}$.

Wa93- ϵ_C exhibits a higher Poisson rate $Q_{\text{pl}} = 5.95$ counts/ks and smaller power-law index of $\xi = 1.67$ as compared to $Q_{\text{pl,bf}}$ and ξ_{bf} (Fig. 8a,b). This means that Wa93- ϵ_C slightly overproduces the quiescent flux-level and reasonably describes the flux distribution for flaring events. For Wa93- ϵ_{PIC} (Fig. 8c,d), the background quiescent flux completely dominates the flux distribution, as is expected from the lightcurve. Figure 9(a,b) shows that Sa93- ϵ_C exceeds the Sgr A* Poisson rate $Q_{\text{pl,bf}}$ and displays no traces of a power-law flux distribution at high flux levels. Sa93- ϵ_{PIC} exhibits a Poisson rate that is larger than $Q_{\text{pl,bf}}$ by a factor of ~ 2 , with a power-law index $\xi = 2.26$ that is steeper than the measured index ξ_{bf} , indicating that there is an overabundance of high-level fluxes, and few flaring excursions beyond the calculated quiescent level (e.g., the maximum X-ray flare spectrum in Fig. 3d). Overall, only Wa93- ϵ_C provides a decent description of the X-ray flux distribution in Sgr A*.

5 DISCUSSION AND CONCLUSIONS

The flaring activity in Sgr A* observed in the NIR/X-ray bands provides important clues about the physics of particle energisation and acceleration in the inner few gravitational radii around a supermassive black hole. Current sheet layers occur naturally in the turbulent, magnetised regions of the disk and will inevitably lead to magnetic reconnection of field lines. Magnetic reconnection results in thermal heating of both electrons and ions, and accelerates a fraction of the electron population to a non-thermal power-law distribution. The nearest supermassive black hole, Sgr A* is monitored well enough to extract statistical information about the nature of flaring events, e.g., the observed flux distributions and power spectra in the sub-mm, NIR and X-ray wavebands. Here, we take advantage of these measured quantities to test whether the combination of synchrotron emission from non-thermal electrons and disk/jet turbulence can explain the general properties of the flaring events.

GRMHD simulations are able to capture MHD turbulence in addition to accurately describing the effects of general relativity in the extreme gravity of black holes (Sec. 2.1). Ideal GRMHD, by definition, does not include dissipative processes such as particle acceleration and the effects of radiation, and hence, to directly compare our simulations with observations of Sgr A*, we rely on an additional layer of modelling for the electron properties, together with GRRT radiative transfer as a post-processing step (Sec. 2.2). Using this procedure, we calculate the multiwavelength spectra of our GRMHD+GRRT radiative models (Sec. 3.2), scaling the black hole mass and distance to that of Sgr A* with an accretion rate of a few $\times 10^{-8} M_{\odot} \text{ yr}^{-1}$ that provides a reasonable fit for the observed sub-mm flux. Further, to study the variability of our simulation lightcurves, we derive the power spectra and cumulative distribution functions in 3 wavelengths: 230 GHz (sub-mm), 2.12 μm (NIR) and 2-8 keV (X-rays) and compare with their observed coun-

terparts (Dexter et al. 2014; Neilsen et al. 2015; Witzel et al. 2018, (Sec. 4)).

We find that one of our models, Wa93- ϵ_C , describes the data reasonably well: (1) the mean spectrum is within observational quiescent limits, (2) the brightest flare X-ray luminosity matches the average X-ray flare spectrum from Neilsen et al. (2015), and (3) the X-ray lightcurve is quite variable and the calculated CDF resembles Sgr A*'s X-ray CDF. However, Wa93- ϵ_C 's brightest flare X-ray luminosity is 25 times smaller than the Haggard et al. (2019) *Chandra* flare. Further, the X-ray lightcurve does not look similar to observed lightcurves, where flares usually span over longer timescales as compared to the flares obtained from our models. This could be a result of using the “fast-light” approximation in our GRRT method, which could become invalid in the vicinity of the black hole, where photon travel time becomes comparable to the timescale at which the plasma distribution changes (e.g., Ball et al. 2020). The NIR CDF follows a log-normal + power-law-like distribution as expected from observations, but has a lower quiescent flux level than that measured for Sgr A*. This model has a relatively weak magnetic flux content in the disk, otherwise known as the “standard and normal evolution” (SANE) model, as opposed to near-magnetically arrested strong field models. The strong field models, on average, overproduce the quiescent X-ray limits and exhibit a lower level of variability in the X-ray lightcurves as compared to Sgr A*. Thus we favour disk turbulence in SANE models as a reasonable mechanism for explaining Sgr A*'s average flare properties.

None of our models can account for the extremely bright NIR flaring reported in Do et al. (2019), though we do achieve moderately high fluxes. There are three possible explanations as to why. It is probable that one needs a pronounced increase in the accretion rate to explain these flares, as suggested by Do et al. (2019). If we consider the strong field model Sa93- ϵ_{PIC} , changes in the accretion primarily drive fluctuating flux levels as seen from the variation in the spectrum (grey region in Fig. 3d) and the brightest X-ray flare spectrum, where the sub-mm and NIR flux both increase by a factor of ~ 2 with respect to the mean spectrum. One other possibility is that turbulence-driven variability is not enough to explain isolated high luminosity events, and that GRMHD simulations with enough resolution to capture plasmoid formation are required instead. Indeed, as Gutiérrez et al. (2020) suggests, a sufficiently strong non-thermal event may be able to explain the Do et al. (2019) observations. However, the resemblance between our calculated CDFs and the measured CDF from Do et al. (2019) suggests that processes that frequently occur in the disk and the jet sheath, such as magnetic reconnection in current sheets, drive most moderate level NIR flux events (also see Petersen & Gammie 2020). A third possibility is the uncertainty in our assumed electron temperature model, i.e., the turbulent-heating motivated $R_{\text{high}} - R_{\text{low}}$ electron temperature model from Howes (2010); Mościbrodzka et al. (2016). There are alternate electron temperature prescriptions (e.g., Mościbrodzka et al. 2009; Dexter et al. 2010; Anantua et al. 2020) as well as electron heating models that consider magnetic reconnection and plasma turbulence (Rowan et al. 2017; Werner et al. 2018; Kawazura et al. 2019; Zhdankin et al. 2019). Indeed, recent work by Dexter et al. (2020b) shows that the radio-to-NIR spectrum depends significantly on whether the electrons get heated by turbulence (Howes 2010) or reconnection (Werner et al. 2018). Similar to our weak field models, Dexter et al. (2020b) finds high rms% in the NIR, though the NIR emission originates from only thermal electrons. Interestingly, they also find that heating due to reconnection offers higher variability. Finally, they favour a magnetically arrested disk

(MAD) model with reconnection-based electron heating, as weak field models fail to produce the observed linear polarisation fraction. MAD disk models offer an interesting alternate source of variability: magnetic eruptions (e.g., Tchekhovskoy et al. 2011) that lead to significant changes in the disk and jet morphology, and contribute to the NIR variability (Dexter et al. 2020a; Porth et al. 2020). Further, recent simulations of the large scale evolution of the accretion flow starting from the Bondi sphere up to the event horizon by Ressler et al. (2020) also favour a large magnetic flux near the black hole of Sgr A*. However, MAD models are difficult to motivate due to the apparent absence of a strong jet in Sgr A*. In this work, our goal is to examine variability due to turbulence-driven reconnection in relatively-stable disks, and hence, we leave an exploration of MADs for future work.

Other alternate sources of variability include radiative cooling (e.g., Fragile & Meier 2009; Dibi et al. 2012; Yoon et al. 2020), jet-wind boundary instabilities (e.g., McKinney 2006; Bromberg & Tchekhovskoy 2016; Chatterjee et al. 2019) and misalignment between the black hole spin vector and the disk angular momentum vector (Dexter & Fragile 2013; White et al. 2020; Chatterjee et al. 2020). It is possible that our conclusions may change with the addition of radiative cooling within the GRMHD simulation. Synchrotron and inverse Compton cooling removes internal energy from the gas and changes the dynamics of the turbulence, thereby altering the disk density and temperature profile, even for accretion rates similar to Sgr A* (Yoon et al. 2020). Hence, if the electron temperature and the acceleration efficiency in the disk current sheets become small enough to satisfy the quiescent NIR and X-ray limits, strong field models might become a viable option. Indeed, in strong field models, collisions between the jet and the disk-wind/environment can lead to pinch and kink mode instabilities that efficiently dissipate magnetic energy as heat and/or accelerate particles, as well as lead to enhanced gas entrainment into the jet (e.g., Chatterjee et al. 2019). Therefore, these jet boundary instabilities could affect the radiative output across the electromagnetic spectrum. Finally, misalignment between the black hole spin and the disk may lead to possible turbulent heating events as well as enhanced jet-wind collisions (Dexter & Fragile 2013; White et al. 2020; Chatterjee et al. 2020). Advanced models of electron thermodynamics and non-conventional disk geometries will no doubt contribute not only to the overall variability of Sgr A* across its entire multiwavelength emission, but also inform our interpretation of the upcoming 230 GHz Event Horizon Telescope image of Sgr A*. This work is meant to be a first study of non-thermal activity in high resolution 3D GRMHD simulations and further exploration of GRMHD simulations with alternate black hole spins, disk/jet morphologies and orientations, imaged at a variety of inclination angles are required to constrain the possible parameter space of Sgr A* models.

In conclusion, this work presents the first studies comparing NIR/X-ray statistics, produced with the best available dynamical models of Sgr A*, to the observations, focusing on variability due to turbulence-driven reconnection. We perform GRRT radiative transfer calculations on two 3D GRMHD models of accreting black holes, one with a weakly magnetised disk and the other a strong field case, using two different realisations of a hybrid thermal+non-thermal electron energy distribution, and generate 230 GHz, 2.12 μ m and 2-8 keV lightcurves over a period of time exceeding 60 hours. A summary of our results are as follows:

(i) Weakly magnetised disks exhibit high levels of variability in the NIR and the X-rays, similar to observations of Sgr A*. Non-

thermal synchrotron emission from disk and jet current sheet layers dominates the NIR-to-X-ray spectrum.

(ii) Non-thermal synchrotron emission due to disk turbulence in weak field models explain the average X-ray flare spectrum and flux distribution of Sgr A* reasonably well.

(iii) Strongly magnetised disks exhibit low variability as highly magnetised plasma is more abundantly found in the disk and jet sheath. Synchrotron emission from both thermal and non-thermal electron populations contribute to the NIR flux while X-rays originate from non-thermal electrons.

(iv) Disk turbulence alone cannot explain recently detected highly luminous Sgr A* NIR and X-ray flares.

From our study, it is apparent that we require simulations that are able to resolve the tiny length-scales of plasmoids in order to explain the bright flares seen in Do et al. (2019) and Haggard et al. (2019). We have seen 2D versions of such simulations only recently (Nathanail et al. 2020; Ripperda et al. 2020). These simulations suggest that we require grid resolutions in excess of 2000 cells across the disk height to trigger the plasmoid instability, indicating that 3D simulations would push us to the brink of computational limitations. It is, however, encouraging to note that our results indicate that one can rely on resolutions similar to this paper to study MHD turbulence-driven variability as a source of moderate level flares in Sgr A*.

ACKNOWLEDGEMENTS

This research was made possible by NSF PRAC awards no. 1615281 and OAC-1811605 at the Blue Waters sustained-petascale computing project and supported in part under grant no. NSF PHY-1125915. This research was enabled in part by support provided by Calcul Quebec (<http://www.calculquebec.ca>) and Compute Canada (<http://www.computecanada.ca>). KC, SM and DY are supported by the Netherlands Organization for Scientific Research (NWO) VICI grant (no. 639.043.513), ZY is supported by a Leverhulme Trust Early Career Research Fellowship, MK is supported by the NWO Spinoza Prize, AT by Northwestern University and by National Science Foundation grants AST-1815304, AST-1911080, and AI by a Royal Society University Research Fellowship. DH acknowledges support from the Natural Sciences and Engineering Research Council of Canada (NSERC) Discovery Grant, the Canada Research Chairs program, and the Canadian Institute for Advanced Research (CIFAR). This research has made use of NASA's Astrophysics Data System.

DATA AVAILABILITY

Data used to plot the images in this work is uploaded at: Zenodo link

REFERENCES

- An T., Goss W. M., Zhao J.-H., Hong X. Y., Roy S., Rao A. P., Shen Z. Q., 2005, *ApJ*, **634**, L49
- Anantua R., Ressler S., Quataert E., 2020, *MNRAS*, **493**, 1404
- Baganoff F. K., et al., 2001, *Nature*, **413**, 45
- Baganoff F. K., et al., 2003, *ApJ*, **591**, 891
- Balbus S. A., Hawley J. F., 1991, *ApJ*, **376**, 214
- Ball D., Özel F., Psaltis D., Chan C.-k., 2016, *ApJ*, **826**, 77
- Ball D., Sironi L., Özel F., 2018, *ApJ*, **862**, 80

Ball D., Özel F., Christian P., Chan C.-K., Psaltis D., 2020, arXiv e-prints, [p. arXiv:2005.14251](https://arxiv.org/abs/2005.14251)

Barrière N. M., et al., 2014, *ApJ*, **786**, 46

Boehle A., et al., 2016, *ApJ*, **830**, 17

Bower G. C., Wright M. C. H., Falcke H., Backer D. C., 2003, *ApJ*, **588**, 331

Bower G. C., et al., 2015, *ApJ*, **802**, 69

Bower G. C., et al., 2019, *ApJ*, **881**, L2

Boyce H., et al., 2019, *ApJ*, **871**, 161

Brinkerink C. D., et al., 2015, *A&A*, **576**, A41

Broderick A. E., McKinney J. C., 2010, *ApJ*, **725**, 750

Bromberg O., Tchekhovskoy A., 2016, *MNRAS*, **456**, 1739

Chael A., Narayan R., Sadowski A., 2017, *MNRAS*, **470**, 2367

Chael A., Rowan M., Narayan R., Johnson M., Sironi L., 2018, *MNRAS*, **478**, 5209

Chan C.-k., Psaltis D., Özel F., Medeiros L., Marrone D., Sadowski A., Narayan R., 2015, *ApJ*, **812**, 103

Chatterjee K., Liska M., Tchekhovskoy A., Markoff S. B., 2019, *MNRAS*, **490**, 2200

Chatterjee K., et al., 2020, *MNRAS*, **499**, 362

Connors R. M. T., et al., 2017, *MNRAS*, **466**, 4121

Davelaar J., Mościbrodzka M., Bronzwaer T., Falcke H., 2018, *A&A*, **612**, A34

Davelaar J., et al., 2019, *A&A*, **632**, A2

Degenaar N., Wijnands R., Miller J. M., Reynolds M. T., Kennea J., Gehrels N., 2015, *Journal of High Energy Astrophysics*, **7**, 137

Dexter J., Fragile P. C., 2013, *MNRAS*, **432**, 2252

Dexter J., Agol E., Fragile P. C., 2009, *ApJ*, **703**, L142

Dexter J., Agol E., Fragile P. C., McKinney J. C., 2010, *ApJ*, **717**, 1092

Dexter J., McKinney J. C., Agol E., 2012, *MNRAS*, **421**, 1517

Dexter J., Kelly B., Bower G. C., Marrone D. P., Stone J., Plambeck R., 2014, *MNRAS*, **442**, 2797

Dexter J., et al., 2020a, arXiv e-prints, [p. arXiv:2006.03657](https://arxiv.org/abs/2006.03657)

Dexter J., et al., 2020b, *MNRAS*, **494**, 4168

Dibi S., Drappeau S., Fragile P. C., Markoff S., Dexter J., 2012, *MNRAS*, **426**, 1928

Dibi S., Markoff S., Belmont R., Malzac J., Barrière N. M., Tomsick J. A., 2014, *MNRAS*, **441**, 1005

Dibi S., Markoff S., Belmont R., Malzac J., Neilsen J., Witzel G., 2016, *MNRAS*, **461**, 552

Do T., et al., 2019, *ApJ*, **882**, L27

Dodds-Eden K., et al., 2009, *ApJ*, **698**, 676

Dodds-Eden K., Sharma P., Quataert E., Genzel R., Gillessen S., Eisenhauer F., Porquet D., 2010, *ApJ*, **725**, 450

Doeleman S. S., et al., 2008, *Nature*, **455**, 78

Drappeau S., Dibi S., Dexter J., Markoff S., Fragile P. C., 2013, *MNRAS*, **431**, 2872

EHTC et al., 2019a, *ApJ*, **875**, L1

EHTC et al., 2019b, *ApJ*, **875**, L5

Eckart A., et al., 2004, *A&A*, **427**, 1

Falcke H., Goss W. M., Matsuo H., Teuben P., Zhao J.-H., Zylka R., 1998, *ApJ*, **499**, 731

Falcke H., Melia F., Agol E., 2000, *ApJ*, **528**, L13

Fishbone L. G., Moncrief V., 1976, *ApJ*, **207**, 962

Fragile P. C., Meier D. L., 2009, *ApJ*, **693**, 771

Gammie C. F., Popham R., 1998, *ApJ*, **498**, 313

Genzel R., Eisenhauer F., Gillessen S., 2010, *Reviews of Modern Physics*, **82**, 3121

Ghez A. M., Salim S., Hornstein S. D., Tanner A., Lu J. R., Morris M., Becklin E. E., Duchêne G., 2005, *ApJ*, **620**, 744

Ghez A. M., et al., 2008, *ApJ*, **689**, 1044

Gillessen S., et al., 2017, *ApJ*, **837**, 30

Gravity Collaboration et al., 2018a, *A&A*, **615**, L15

Gravity Collaboration et al., 2018b, *A&A*, **618**, L10

Gravity Collaboration et al., 2020a, arXiv e-prints, [p. arXiv:2004.07185](https://arxiv.org/abs/2004.07185)

Gravity Collaboration et al., 2020b, *A&A*, **635**, A143

Guo F., Li H., Daughton W., Liu Y.-H., 2014, *Phys. Rev. Lett.*, **113**, 155005

Gutiérrez E. M., Nemmen R., Cafardo F., 2020, *ApJ*, **891**, L36

Haggard D., et al., 2019, *ApJ*, **886**, 96

Hawley J. F., Guan X., Krolik J. H., 2011, *ApJ*, **738**, 84

Hornstein S. D., Matthews K., Ghez A. M., Lu J. R., Morris M., Becklin E. E., Rafelski M., Baganoff F. K., 2007, *ApJ*, **667**, 900

Houck J. C., Denicola L. A., 2000, in Manset N., Veillet C., Crabtree D., eds, *Astronomical Society of the Pacific Conference Series* Vol. 216, *Astronomical Data Analysis Software and Systems IX*, p. 591

Howes G. G., 2010, *MNRAS*, **409**, L104

Issaoun S., Johnson M. D., Blackburn L., et al., 2019, *ApJ*, **871**, 30

Kawazura Y., Barnes M., Schekochihin A. A., 2019, *Proceedings of the National Academy of Science*, **116**, 771

Leung P. K., Gammie C. F., Noble S. C., 2011, *ApJ*, **737**, 21

Liska M., Hesp C., Tchekhovskoy A., Ingram A., van der Klis M., Markoff S., 2018, *MNRAS*, **474**, L81

Liska M., et al., 2019, arXiv e-prints, [p. arXiv:1912.10192](https://arxiv.org/abs/1912.10192)

Lu R. S., Krichbaum T. P., Zensus J. A., 2011, *MNRAS*, **418**, 2260

Markoff S., 2005, *ApJ*, **618**, L103

Markoff S., Falcke H., Yuan F., Biermann P. L., 2001, *A&A*, **379**, L13

Markoff S., Bower G. C., Falcke H., 2007, *MNRAS*, **379**, 1519

Marrone D. P., Moran J. M., Zhao J.-H., Rao R., 2007, *ApJ*, **654**, L57

Marrone D. P., et al., 2008, *ApJ*, **682**, 373

Matsumoto T., Chan C.-H., Piran T., 2020, arXiv e-prints, [p. arXiv:2004.13029](https://arxiv.org/abs/2004.13029)

McKinney J. C., 2006, *MNRAS*, **368**, 1561

Melia F., Falcke H., 2001, *ARA&A*, **39**, 309

Mościbrodzka M., Falcke H., 2013, *A&A*, **559**, L3

Mościbrodzka M., Gammie C. F., Dolence J. C., Shiokawa H., Leung P. K., 2009, *ApJ*, **706**, 497

Mościbrodzka M., Falcke H., Shiokawa H., 2016, *A&A*, **586**, A38

Narayan R., Igumenshchev I. V., Abramowicz M. A., 2003, *PASJ*, **55**, L69

Nathanail A., Fromm C. M., Porth O., Olivares H., Younsi Z., Mizuno Y., Rezzolla L., 2020, *MNRAS*, **495**, 1549

Neilsen J., et al., 2013, *ApJ*, **774**, 42

Neilsen J., et al., 2015, *ApJ*, **799**, 199

Nord M. E., Lazio T. J. W., Kassim N. E., Hyman S. D., LaRosa T. N., Brogan C. L., Duric N., 2004, *AJ*, **128**, 1646

Nowak M. A., et al., 2012, *ApJ*, **759**, 95

Özel F., Psaltis D., Narayan R., 2000, *ApJ*, **541**, 234

Petersen E., Gammie C., 2020, *MNRAS*, **494**, 5923

Ponti G., et al., 2017, *MNRAS*, **468**, 2447

Porth O., Chatterjee K., Narayan R., et al., 2019, *ApJS*, **243**(2), 40pp

Porth O., Mizuno Y., Younsi Z., Fromm C. M., 2020, arXiv e-prints, [p. arXiv:2006.03658](https://arxiv.org/abs/2006.03658)

Quataert E., 2002, *ApJ*, **575**, 855

Quataert E., Narayan R., 1999, *ApJ*, **520**, 298

Reid M. J., et al., 2019, *ApJ*, **885**, 131

Ressler S. M., Tchekhovskoy A., Quataert E., Chandra M., Gammie C. F., 2015, *MNRAS*, **454**, 1848

Ressler S. M., Tchekhovskoy A., Quataert E., Gammie C. F., 2017, *MNRAS*, **467**, 3604

Ressler S. M., White C. J., Quataert E., Stone J. M., 2020, arXiv e-prints, [p. arXiv:2006.00005](https://arxiv.org/abs/2006.00005)

Ripperda B., Bacchini F., Philippov A., 2020, arXiv e-prints, [p. arXiv:2003.04330](https://arxiv.org/abs/2003.04330)

Rowan M. E., Sironi L., Narayan R., 2017, *ApJ*, **850**, 29

Roy S., Pramesh Rao A., 2004, *MNRAS*, **349**, L25

Ryan B. R., Ressler S. M., Dolence J. C., Tchekhovskoy A., Gammie C., Quataert E., 2017, *ApJ*, **844**, L24

Schödel R., Morris M. R., Muzic K., Alberdi A., Meyer L., Eckart A., Gezari D. Y., 2011, *A&A*, **532**, A83

Serabyn E., Carlstrom J., Lay O., Lis D. C., Hunter T. R., Lacy J. H., Hills R. E., 1997, *ApJ*, **490**, L77

Shcherbakov R. V., Penna R. F., McKinney J. C., 2012, *ApJ*, **755**, 133

Sironi L., Spitkovsky A., 2014, *ApJ*, **783**, L21

Sironi L., Petropoulou M., Giannios D., 2015, *MNRAS*, **450**, 183

Tchekhovskoy A., Narayan R., McKinney J. C., 2011, *MNRAS*, **418**, L79

Verner D. A., Ferland G. J., Korista K. T., Yakovlev D. G., 1996, *ApJ*, **465**, 487

Wang Q. D., et al., 2013, [Science](#), **341**, 981

Werner G. R., Uzdensky D. A., Begelman M. C., Cerutti B., Nalewajko K., 2018, [MNRAS](#), **473**, 4840

White C. J., Dexter J., Blaes O., Quataert E., 2020, [ApJ](#), **894**, 14

Wilms J., Allen A., McCray R., 2000, [ApJ](#), **542**, 914

Witzel G., et al., 2012, [ApJS](#), **203**, 18

Witzel G., et al., 2018, [ApJ](#), **863**, 15

Xiao F., 2006, [Plasma Physics and Controlled Fusion](#), **48**, 203

Yoon D., Chatterjee K., Markoff S. B., van Eijnatten D., Younsi Z., Liska M., Tchekhovskoy A., 2020, [MNRAS](#), **499**, 3178

Younsi Z., Zhidenko A., Rezzolla L., Konoplya R., Mizuno Y., 2016, [Phys. Rev. D](#), **94**, 084025

Younsi Z., Porth O., Mizuno Y., Fromm C. M., Olivares H., 2020, in Asada K., de Gouveia Dal Pino E., Girotti M., Nagai H., Nemmen R., eds, IAU Symposium Vol. 342, IAU Symposium. pp 9–12 ([arXiv:1907.09196](#)), doi:10.1017/S1743921318007263

Yuan F., Narayan R., 2014, [ARA&A](#), **52**, 529

Yuan F., Markoff S., Falcke H., 2002, [A&A](#), **383**, 854

Yuan F., Quataert E., Narayan R., 2003, [ApJ](#), **598**, 301

Zhang S., et al., 2017, [ApJ](#), **843**, 96

Zhao J.-H., Bower G. C., Goss W. M., 2001, [ApJ](#), **547**, L29

Zhao J.-H., Young K. H., Herrnstein R. M., Ho P. T. P., Tsutsumi T., Lo K. Y., Goss W. M., Bower G. C., 2003, [ApJ](#), **586**, L29

Zhdankin V., Uzdensky D. A., Werner G. R., Begelman M. C., 2019, [Phys. Rev. Lett.](#), **122**, 055101

Zylka R., Mezger P. G., Ward-Thompson D., Duschl W. J., Lesch H., 1995, [A&A](#), **297**, 83

This paper has been typeset from a $\text{\TeX}/\text{\LaTeX}$ file prepared by the author.